Article:
Valdivia-Camacho, M.A., Cuthill, F., McCarthy, E.D. et al. (2025) Forensic investigation of failure in a full-scale composite tidal turbine blade. Engineering Failure Analysis, 182, Part B. 110076. ISSN: 1350-6307

https://doi.org/10.1016/j.engfailanal.2025.110076

Engineering Failure Analysis 182 (2025) 110076

Contents lists available at ScienceDirect

Engineering Failure Analysis

journal homepage: www.elsevier.com/locate/engfailanal

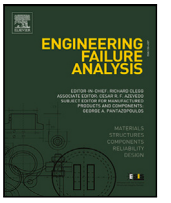

Forensic investigation of failure in a full-scale composite tidal turbine blade

Miguel A. Valdivia-Camacho [a], Fergus Cuthill [a], Edward D. McCarthy [a], Sergio Lopez Dubon [a], Conchúr M. Ó Brádaigh [b], Parvez Alam [a,*]

[a] School of Engineering, The University of Edinburgh, Sanderson Building, Robert Stevenson Road, The King's Buildings, Edinburgh, EH9 3FB, UK

[b] Faculty of Engineering, University of Sheffield, Sir Frederick Mappin Building, Mappin Street, Sheffield, S1 3JD, UK

ARTICLE INFO

Keywords:
Tidal energy
Composite blades
Mechanical testing
Failure

ABSTRACT

Tidal turbine blades endure uniquely harsh, shear-dominated loads that distinguish them from wind turbines, yet their failure mechanisms remain poorly understood. In this study, we report the first full-scale failure investigation of a tidal blade made of glass fibre reinforced polymer (GFRP), carbon fibre reinforced polymer (CFRP) and cast iron. The blade was subjected to 26 static tests and 17 fatigue tests using a bespoke laboratory setup with three hydraulic actuators and saddle fixtures. Strain gauges, displacement transducers, and digital image correlation (DIC) were coupled to track local deformation and damage. Artificial defects accelerated damage progression, yielding roughly 97,000 fatigue cycles before ultimate failure. Two dominant failure modes emerged: de-bonding between the pressure skin and root connection under quasi-static loading at 216 % of design load, and bondline failure between pressure and suction skins under fatigue at 119 % of design load. A subsequent static test showed residual strength drop to only 68.8 % of the original design load. These findings highlight the critical role of bond interfaces in blade integrity and the contribution of internal ribs in maintaining structural performance. While local stiffness was affected by damage, global stiffness remained largely intact, reinforcing the importance of investigating long-term performance degradation and failure evolution in tidal turbine blades.

1. Introduction

Tidal stream turbines represent a viable and increasingly supported renewable energy technology, with growing interest from both public and private sectors. In the UK alone, recent government funding has supported five new tidal projects, adding 28 MW of the 130 MW expected to be connected to the national grid by 2029 [1]. As investment grows, so does the demand for reliable and cost-effective turbine designs capable of withstanding the extreme and complex marine environment. Turbine blades remain one of the most critical and failure-prone structural components of a tidal turbine [2], making them a central focus for ongoing design, manufacturing, and testing efforts. However, despite extensive design optimisation and feasibility studies, full-scale experimental investigations of tidal blade failure mechanisms are conspicuously absent.

Much of the existing research has concentrated on optimising the hydrodynamic performance of tidal blades, primarily through computational fluid dynamics (CFD) [3]. Underwater effects such as cavitation and biofouling pose major concerns as tidal blades are difficult to maintain or repair once deployed [4]. In response, studies have explored the development of improved blade profiles

* Corresponding author.
E-mail address: parvez.alam@ed.ac.uk (P. Alam).

https://doi.org/10.1016/j.engfailanal.2025.110076
Received 27 June 2025; Received in revised form 12 August 2025; Accepted 1 September 2025
Available online 13 September 2025

by combining conventional hydrofoils with machine learning techniques, optimising parameters such as chord length and pitch angle [5]. Collectively, these efforts have enhanced power extraction capabilities under varying flow conditions, contributing to more efficient turbine designs.

Despite these hydrodynamic advances, tidal blades face structural challenges that distinguish them from their wind counterparts. Operating in a denser medium, tidal blades experience substantially higher loads over shorter spans, necessitating stiffer and thicker structural profiles [6]. This requirement increases reliance on composite materials, particularly in the spar caps, where higher thicknesses of glass fibre reinforced polymers (GFRP) and carbon fibre reinforced polymers (CFRP) are commonly used [7]. While wind turbine blades have been extensively studied at full scale, the structural performance of tidal blades remains its relevancy. This limited research focus is largely due to most tidal turbines remaining at the prototype stage, where design efforts have prioritised the overall system performance over long-term operational reliability.

Most existing failure analyses have been conducted at the coupon level, leaving significant gaps in understanding how full-scale tidal blades behave under complex loading scenarios. For instance, both CFRP and GFRP samples showed a change in failure modes after a certain ageing duration [8,9]. Composite-aluminium interfaces are studied in fatigue as these showed debonding mechanisms in root joints [10]. Simulations suggest that buckling is a primary concern in tidal blades, often mitigated by increasing the thickness-to-chord ratio [11]. The leading edge has been identified as particularly susceptible to local buckling [12], while shear web failures have also been predicted in simulation studies [13].

In contrast, full-scale testing of wind turbine blades has offered detailed insights into typical failure modes. For instance, a 52.3 m wind blade tested under static loading exhibited multiple damage mechanisms including delamination, laminate fracture, and skin-core debonding, with initial failure occurring near the trailing edge [14]. This pattern has been corroborated in other studies involving 14.3 m [15,16] and 34 m blades [17,18], where surface cracks, bondline failures, and skin debonding near the trailing edge were consistently observed. Trailing edge debonding has also been linked to global torsional failure in longer blades [19], and finite element (FE) models have been employed to evaluate the criticality of bonding in that region [20,21]. The transition zone between the root and airfoil cross-sections has been particularly prone to damage initiation [22], while buckling-driven delamination has been documented in blades subjected to mixed loading scenarios [23,24]. Even under fatigue loading, failure often initiates with delamination at the root or suction side of the skin, progressing through buckling to complete structural loss [25].

Advanced numerical models were also used that highlight delamination between composite plies as a key failure mechanism in wind turbine blades, especially when initiated near surface layers [18], where localised out-of-plane deflections can further drive buckling in the skin [26] and the shear webs [27,28]. These effects are often exacerbated by compressive stresses, shear loading [29], and geometric imperfections [30], such as ply drops and material transitions [31].

By comparison, very few full-scale tests have probed tidal blades' structural failure mechanisms directly. Instead, researchers reported no damage and have primarily investigated related topics such as manufacturing defects [32], fatigue and load transfer methods [33], and finite element model validation [34]. Others have focused on hub connections and setup flexibility at loads beyond design limits [35], quality assurance in blade design [36,37], and the validation of test frames [38,39] and loading mechanisms specifically for tidal blades [40,41]. The main test standards available for tidal turbine blades, IEC TS 62600-3 [42] and DNV GL-ST-0164 [43], were adapted directly from certifications originally developed for wind turbine blades. Consequently, it remains unclear whether tidal blades follow the same failure pathways as wind turbine blades or whether their unique shear dominated loading gives rise to distinct damage modes.

This study tests the hypothesis that full-scale tidal turbine blades exhibit failure mechanisms distinct from wind turbine blades due to their unique geometry, steep thickness gradient and shear dominated loading. To investigate this, we perform a comprehensive failure analysis of a full-scale tidal turbine blade under both static and fatigue loading. Damage initiation and progression across multiple test cases is monitored using digital image correlation (DIC), strain measurements, and post-failure microscopy. This work aims to understand how adhesive bond lines, internal structural components, and manufacturing variability critically influence tidal blades' long-term performance and design reliability.

2. Methods

2.1. Tidal turbine blade design specifications

This study tested a 5.25 m composite blade that was part of a 500 kW DeepGen tidal turbine deployed in Orkney, UK in 2010, as seen in Fig. 1a. Only one full scale blade was tested, reflecting both access constraints from the lending organisation and the substantial time and resource demands of a full failure campaign. The manufacture of a full scale blade can cost hundreds of thousands, making destructive testing economically demanding. Information regarding its design, internal structure, manufacturing process, and material properties was limited by the involved companies. However, the material systems and assembly procedures are representative of tidal blades, as this design drew on proven wind industry materials at the time of manufacture. The outer geometry of the blade was mapped using a 3D scan and several NACA 62XXX profiles were matched accordingly. Fig. 1b shows a top view of the blade, starting with a circular root that transitions to different airfoils in a tapered profile. The hydrodynamic performance of this blade has been further analysed using a CFD approach in [39], using velocity profiles from on-site tidal current measurements [44].

The Deepgen tidal blade is built similarly to wind turbine blades, with the components mentioned in Table 1 using different materials based on their main structural role. The skins, made of 8 mmthick glass fibre (+/−45° UD prepreg), cover the top and bottom surfaces, resisting pressure forces and torsion while enhancing impact resistance [45]. These skins are joined at the leading

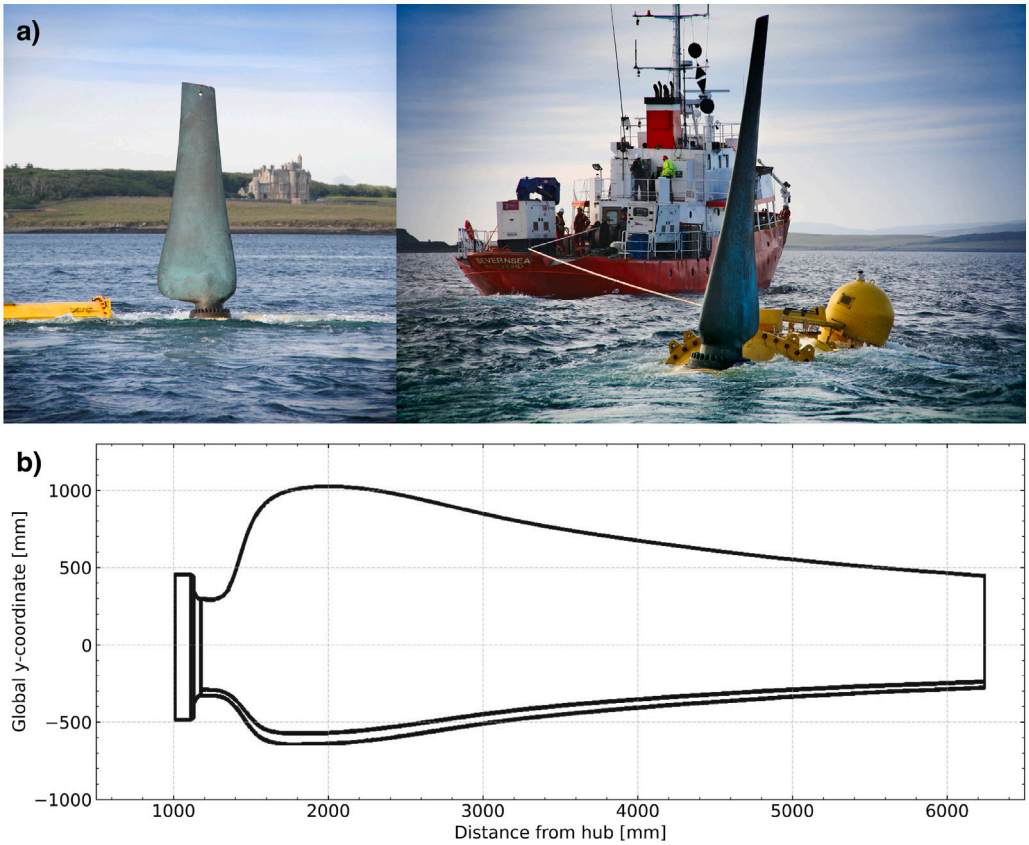

Fig. 1. DeepGen III tidal turbine: (a) Prior to first deployment [45]; (b) plan view of the 5.25 m blade.

Table 1
Materials used in each of the blade components.

Blade component	Material
Root connection	Cast iron
Spar	CFRP UD
Webs	CFRP UD
Rear spar	GFRP Woven
Ribs	GFRP Woven
Skin	GFRP UD

edge with a joggle lap joint and bonded at the trailing edge with a toughened acrylic adhesive. Internally, 6 mm thick glass fibre ribs, positioned along the blade length, transfer shear loads from the skins to the spar. The central spar consists of carbon fibre spar caps (80% UD fibre) that primarily resist flapwise bending moments, with additional cross fibres (0/90° woven fabric) ensuring shear bond strength. Carbon fibre shear webs (+/−45° prepreg) reinforce the spar against shear forces, while an optional foam fill may provide additional support. A glass fibre rear spar, located approximately 100 mm from the trailing edge, mitigates peel stresses. At the root, a spheroidal graphite iron (SGI) casting, bonded to the spar, ensures load transfer, with its tapered geometry providing structural redundancy in case of bond failure. All internal components were reportedly bonded (see Fig. 2) with epoxy systems Spabond and Ampreg (Gurit, UK), although the specific grades and their joint locations were not documented. The ribs are positioned every 300 mm and consist of two laminates bonded together. Each lamina ends on a wide flange in the z-direction. Lastly, the blade is filled with high density polyurethane foam, which added buoyancy to the structure. Mechanical property data for these materials were not provided in the blade design report. Full mechanical characterisation of the constituent materials will be presented in a follow-up study.

2.2. Experimental setup

Only one full-scale blade was tested, reflecting both constraints from the lending organisation and the substantial time and resource demands of a full failure campaign. The manufacture of a full-scale blade can cost hundreds of thousands, making

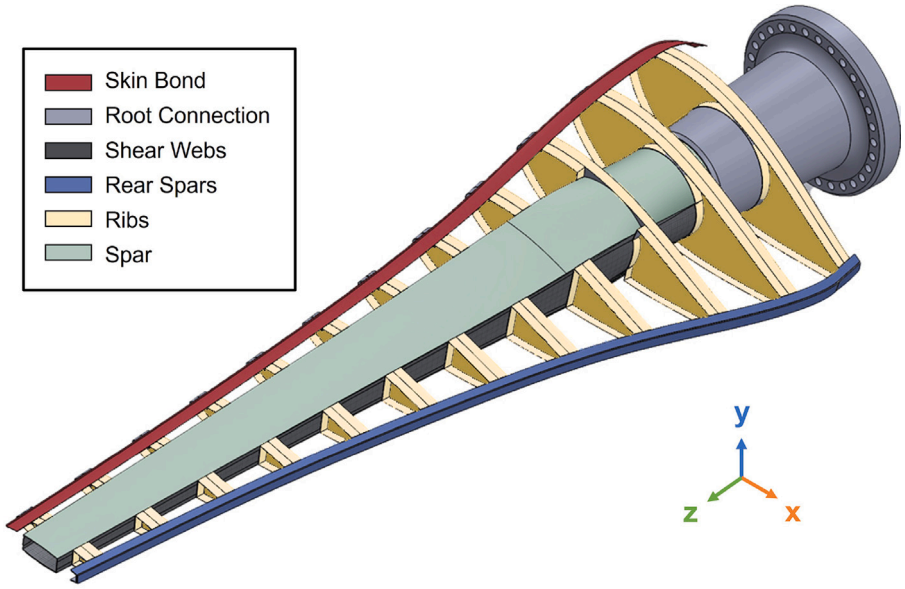

Fig. 2. Isometric view of the internal structure of the tidal blade.

destructive testing economically demanding. The blade is mounted to the test frame shown via a 65 mm interface plate made of S355 structural steel. The pressure distribution was discretised into three point loads located at 2.52 m, 3.57 m and 4.42 m from the root, each applying 94.43 kN via hydraulic actuators during static testing. This optimisation reported in [40] used equivalent hydrodynamic loads from CFD simulations, minimising error in shear force and bending moment distribution while maximising the analysis area away from the saddles, in accordance with IEC TS 62600-3:2020. All hydraulic pistons are connected to the steel frames along the blade's neutral *z*-axis, minimising torsional effects during loading. Alignment with the neutral z axis was maintained across test conditions and verified by live video throughout testing. The fatigue design load was defined by a mean load of 40 kN per actuator and a load amplitude of 25 kN, resulting in fatigue testing under an R-ratio of 0.23. These loading conditions have increased throughout the study to induce failure (see Supplementary Material S.1). Load was transferred from the actuators to the blade surface through an optimised system of steel frames and 200 mm-thick wooden saddles shaped to match the blade's profile [41]. A 2 mm rubber sheet was inserted between the blade and the saddles to increase the contact area and reduce localised stress concentrations caused by surface roughness. The complete experimental setup (Fig. 3) underwent only minor modifications during the testing campaign to safeguard the equipment. For example, the manual torque wrench previously used to tension the saddles was replaced with precise hydraulic bolt tensioners, which reduced slip and improved pressure distribution on the blade surface [41]. In addition, the saddles themselves were upgraded from medium-density fibreboard to plywood, as the latter showed a compressive strength five times higher than MDF.

2.3. Test conditions

Details of each test can be found in Section S.1 of the Supplementary Material, with the test case parameters outlined in Table 2. In the first test, 100% of the design load was applied to the blade to serve as a control test. No change in stiffness was observed during subsequent static and fatigue tests; therefore, damage was introduced into the blade. A generalised finite element model was analysed to identify high stress concentration zones. Fig. 4a shows one of these stress hotspots, located 1200 mm from the root on the neutral *z*-axis of the blade. Case B represents the first testing condition in which damage was introduced, involving the drilling of a 22 mm hole through the skin and the spar at the region of interest identified in Fig. 4b. The diameter of the hole was maximised given the available laboratory resources, prompting stress to extend beyond the local stress domain and provoke a global structural response. Additional cases, in which more damage was manually introduced, are presented in Fig. 5. Test cases D1 and D2 included 300 mm notches that included damage on the shear webs to ensure failure. In the final test condition (Case D2), severe damage was introduced on the pressure side of the blade, which likely increased compressive strain concentrations on the suction side. This asymmetric stiffness degradation could promote buckling-driven delamination, consistent with observations from previous studies where localised compressive strains and geometric imperfections led to suction-side delamination and progressive failure [23,24,30].

A maximum load equivalent to 400% of the design load was applied to the blade during a static test under Case C testing conditions. A total of 26 static tests were conducted, and approximately 96,000 fatigue cycles were completed as part of this study.

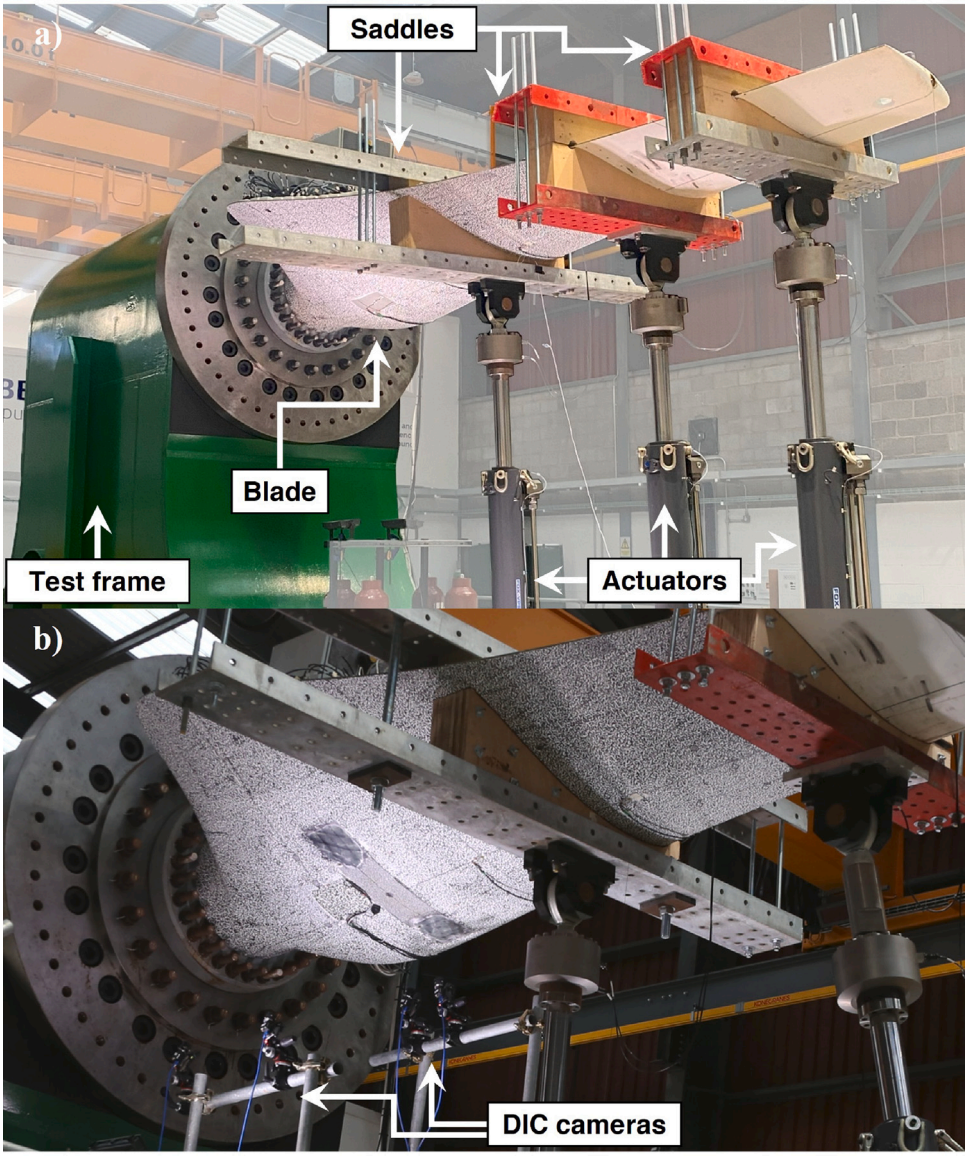

Fig. 3. Comparison of the experimental setup between (a) the first static test; (b) the last static test before failure.

Table 2
Test conditions for the gradually damaged tidal blade.

Test case	Static tests	Fatigue tests	Description
A	2	1	Reference test, no induced damage to the blade.
B	3	4	22 mm hole drilled at 1200 mm from the root, on the neutral z-axis.
C	16	6	Similar to Case B, with 50 mm notches at each side of the hole.
D1	2	3	Similar to Case B, with 300 mm notches at each side of the hole.
D2	3	1	Similar to Case D1, with different speckle pattern for DIC.

The resulting root bending moments from all static tests, as well as the corresponding reduction in shear force under different test conditions, are presented in Fig. 6. A root bending moment of 2.3 MN m was reached in static test 18, corresponding to a shear force of 657.86 kN at the root. These values do not account for potential damage that may have been introduced during blade deployment or transportation prior to the experiments. Modal tests were also performed to identify any changes in the natural frequency of the blade.

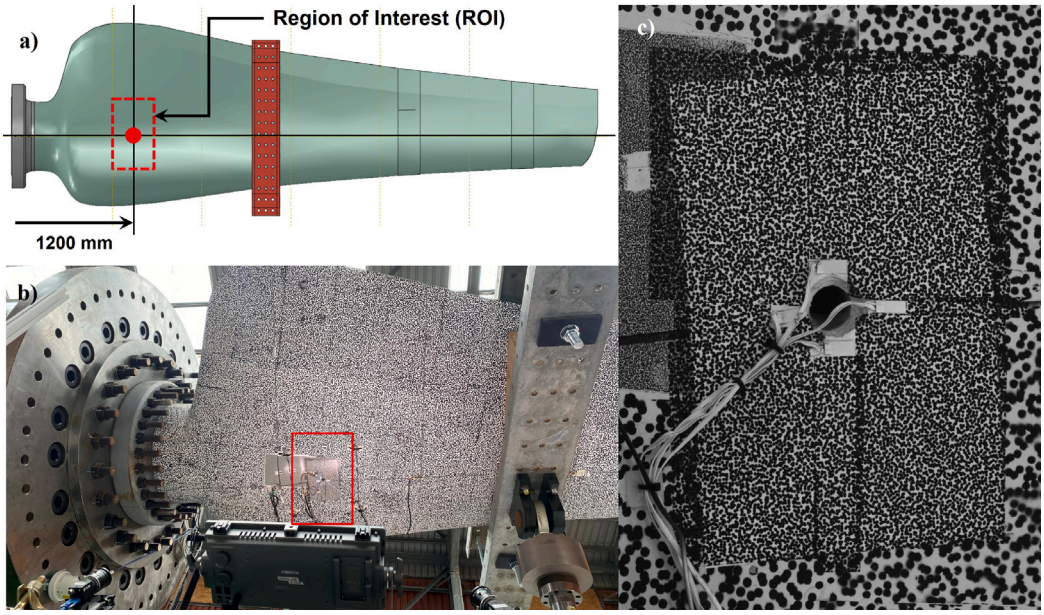

Fig. 4. Pressure side of the blade: (a) Diagram of the hole location; (b) Region of interest (ROI) on the pressure surface of the blade; (c) 22 mm hole location with 4 linear strain gauges.

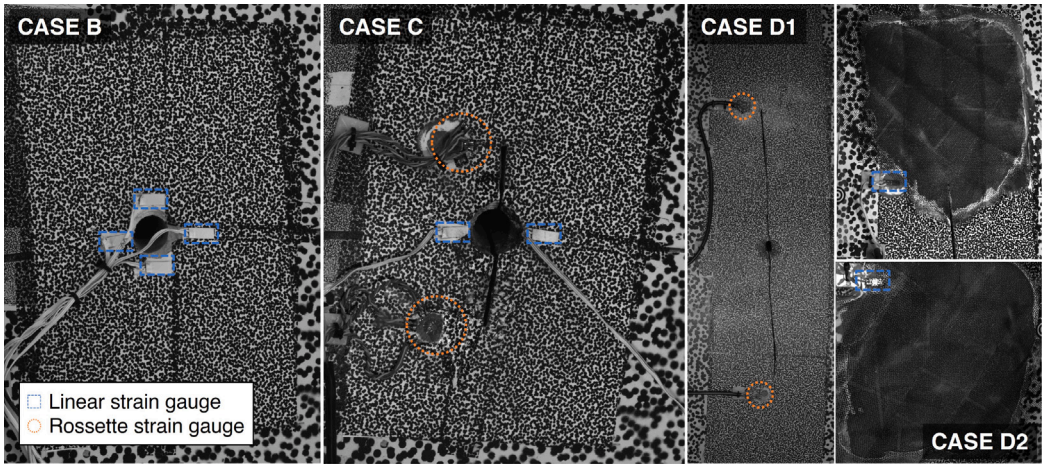

Fig. 5. Test conditions surrounding the initial hole on the surface of the blade. Case D2 shows only the crack tips.

2.4. Instrumentation

Several measurement sensors were installed on the blade surface. Specifically, eight 120 Ω rosette strain gauges were mounted on top of the spar caps, spaced 800 mm apart. Four 350 Ω linear strain gauges were positioned near the leading edge, the trailing edge, and along the skin bond line. The locations of both the rosette and linear strain gauges are shown in Fig. 7. All gauges were zeroed before each test to measure baseline noise, which never exceeded 50 μm m^{-1}. Displacement was measured at the blade tip and at the mid-span along the z-direction. Displacement and force data were also recorded using the load cells. Additional strain gauges were placed around the induced damage sites, as illustrated in Figs. 4c and 5. Further instrumentation, including strain gauges, accelerometers, and thermocouples, was installed on the test rig and auxiliary equipment to enable continuous structural health monitoring throughout all tests.

Images of the blade's bottom surface were captured using six cameras arranged in pairs, enabling further analysis through Digital Image Correlation (DIC). The skin surface was painted white and randomly speckled with 5 mm black dots, allowing displacement

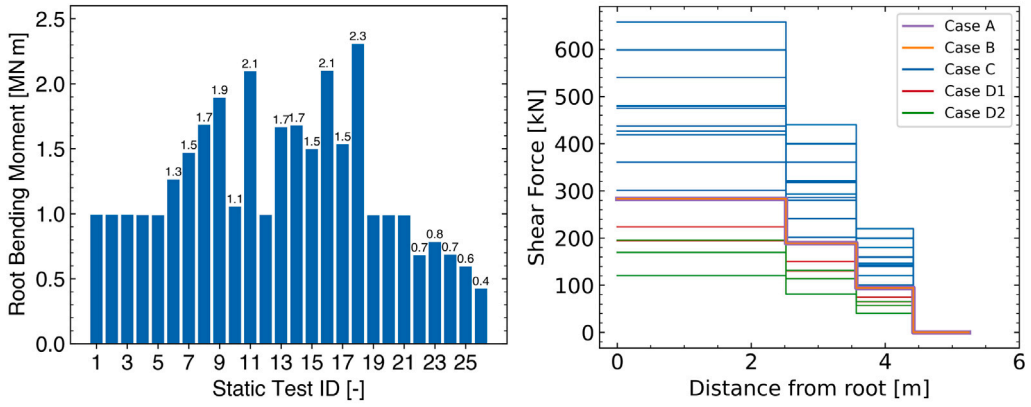

(a) Resulting root bending moment. (b) Shear force diagram.

Fig. 6. Overview of all the three-actuator static tests analysed.

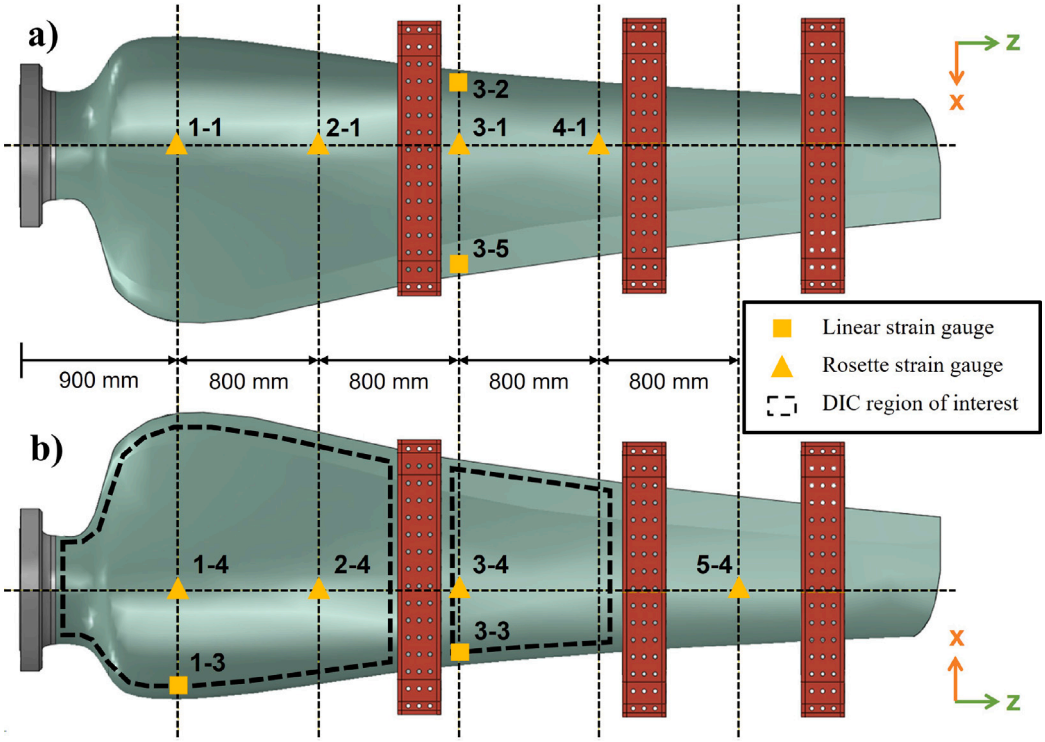

Fig. 7. Initial strain gauge locations and DIC regions of interest (ROI) at: (a) the suction side of the blade; (b) the pressure side of the blade.

and strain to be tracked by the DIC algorithms based on the resulting unique subset patterns. Additionally, we performed a speckle resolution analysis for the DIC cameras focused on the hole and established that a speckle size of 1.9 mm is optimal. The correlation procedure, which was performed prior to each test to account for variations in camera alignment, lighting, and temperature, is shown in Fig. 8. The zero-normalised sum of squared differences (ZNSSD) criterion was selected due to the high variability in lighting conditions throughout the experiments. A step size of 10 pixels was used in all cases, and local bi-cubic splines were applied for interpolation. Strain tensors were computed using the logarithmic Euler–Almansi strain formulation. The strain maps obtained through DIC post-processing were validated using strain gauges installed near the regions of induced damage. Long fatigue tests were conducted in segments to maintain operational accuracy of the equipment, with scheduled pauses to monitor and recalibrate all instrumentation.

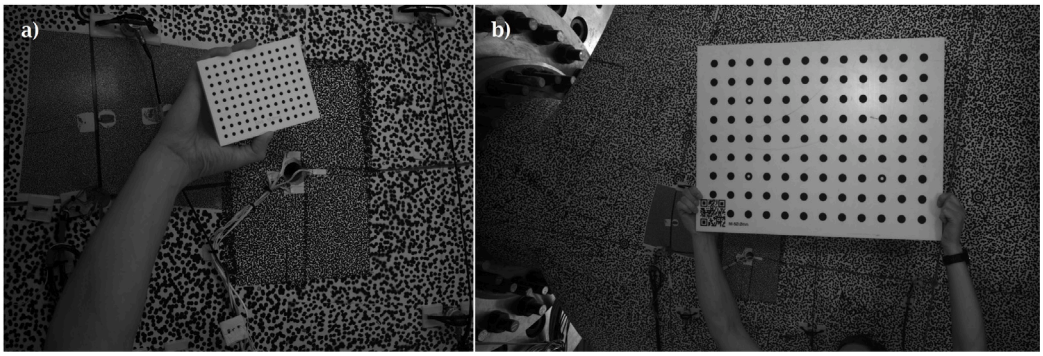

Fig. 8. DIC calibration for different strain resolutions: (a) high-resolution 10 mm spaced dots; (b) 50 mm spaced dots.

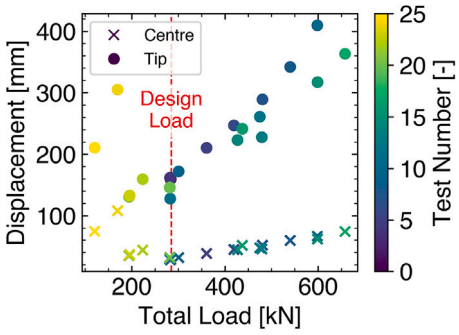

Fig. 9. Load vs. displacement for all static tests. Colour grading represents the test number.

3. Results & discussion

A total of 40 full tests were conducted on the tidal blade, excluding preliminary short tests performed below design loads to verify the data acquisition systems. The duration of the experimental campaign demonstrated the extremely high stiffness of the blade. Fig. 9 presents the total applied load against the displacements recorded at both the centre and tip of the blade. A linear elastic response was observed as the load increased beyond the design value, reaching a maximum of 657.86 kN. Only static tests performed after the two major failure events exhibited deviations from this behaviour. Failure events were identified by abrupt changes in sensor readings during testing.

To compare displacement behaviour under consistent conditions, Fig. 10 shows the displacement at the centre and tip of the blade at a total load of 120 kN (or 40 kN per actuator), as not all static tests were conducted at identical load targets. For the first nine static tests, the introduction of a 22 mm hole (test case B) had negligible effect on the blade's global structural response. Although the hole was not intended to simulate impact damage, these results suggest the blade could remain functional with such a defect, underpinning the challenges of underwater maintenance [4].

Additionally, three critical events are identified in Fig. 10. The first, labelled "A", occurred during static test number 11. A target load of 600 kN was applied via a ramp lasting 20 min, followed by an intended hold phase for 2 min. However, failure occurred in the saddles due to high shear stresses. Further analysis and the adoption of a stiffer plywood saddle material are detailed in [41]. Additionally, the actuators were repositioned to align perpendicularly to the blade's final orientation rather than its initial configuration, in order to minimise second-order moments and reduce saddle slipping. These improvements align with Glennon's concerns about the adaptability of test rigs when loading blades beyond their design limits [35].

Subsequent damage was observed during failure event "B", the first to affect the blade itself. In this case, failure occurred at 617.65 kN after 327.4 s of ramp loading, despite a planned target of 660 kN. The failure was localised near the root section, as shown in Fig. 11b. This failure mode can be described as a root-skin interface debonding, confirming concerns on this adhesive joint raised in Zuo's and Hosseini-Toudeshky's studies on wind turbine blades [10,22].

Finally, failure event "C" marked the ultimate failure of the blade, after which the design load could no longer be sustained. This event occurred between static tests 24 and 25, during a fatigue test conducted slightly above the design fatigue load, with a mean actuator load of 47.5 kN and an amplitude of 27.5 kN. Fig. 11c highlights the final failure feature: pressure–suction skin interface debonding adjacent to the leading edge. Although prior studies have not reported this mode, Bir identified the leading edge as particularly vulnerable to impact in tidal blades [12], underscoring its critical role in structural integrity. Following these events, residual strength tests were conducted to quantify the degradation in stiffness. The next sections present additional analyses of the tests associated with these failure events.

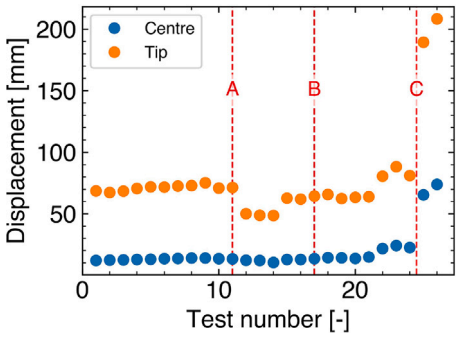

Fig. 10. Displacement at the centre and tip of the blade for all the static tests at 40 kN of load applied per actuator. Dashed lines represent critical events.

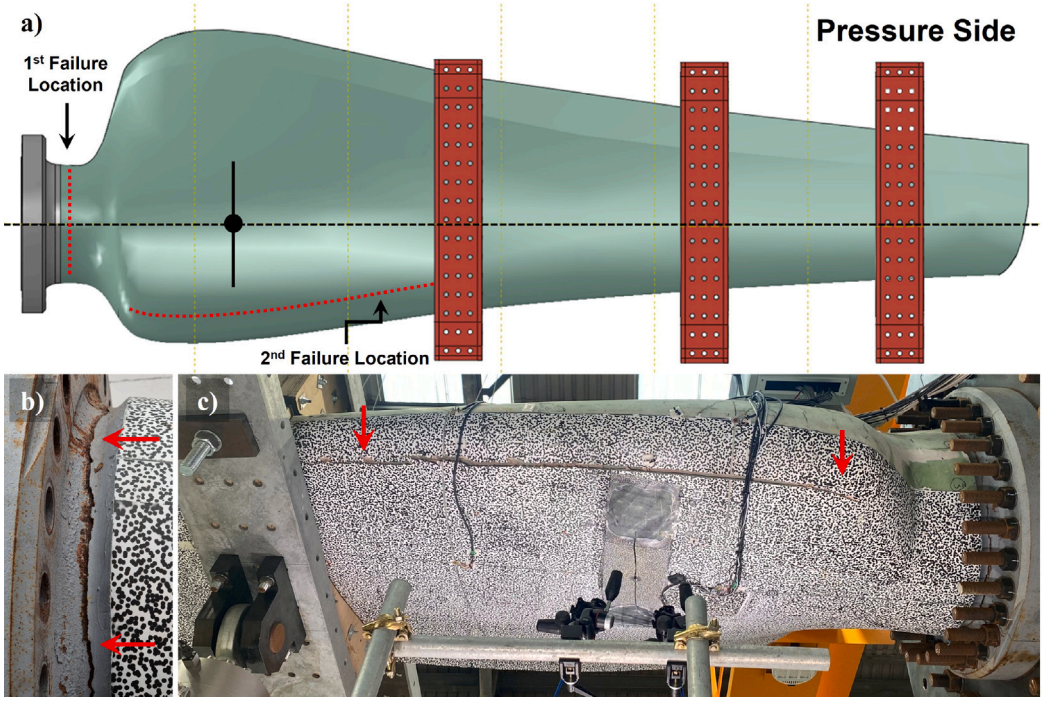

Fig. 11. Diagram on the pressure side of the blade: (a) Location of both failure events; (b) First failure event; (c) Seconds and final failure event.

The strain measurements obtained from the various gauges installed on both sides of the blade are compared in Fig. 12, enabling the identification of the locations of the two failure events and their associated damage progression. Strain gauge 1–1, positioned closest to both failure events on the top surface of the blade, recorded increasing strain magnitudes as additional static tests were performed, indicating the progression of damage in this region. Since the displacement measurements did not exhibit a corresponding trend indicative of global stiffness degradation, it is inferred that the damage was localised and had a direct impact on this area. T

In contrast, the readings from strain gauge 3–5 did not show any significant variation in strain distribution across the different test conditions. However, measurements obtained during the residual strength tests indicated that, following the final blade failure, the rear spar near the trailing edge began to absorb a larger portion of the applied load. Minimal changes in strain distribution were recorded by the remaining strain gauges located on the suction side of the blade, particularly in the region between the first and second actuators.

The pressure side of the blade, as shown in Fig. 12, exhibited a behaviour similar to that of the suction side, where regions located near the drilled hole and the subsequent failure features experienced the most pronounced changes in strain distribution. Strain gauges 3–3 and 5–4 recorded inconsistent data following the first critical event involving saddle failure; however, no changes in local stiffness were observed prior to that point.

Overall, the root failure event did not result in a noticeable alteration in stress distribution, as load transfer from the skin to the spar via the ribs was still maintained. Strain gauge 1–3, positioned closest to the second failure feature, recorded a significant

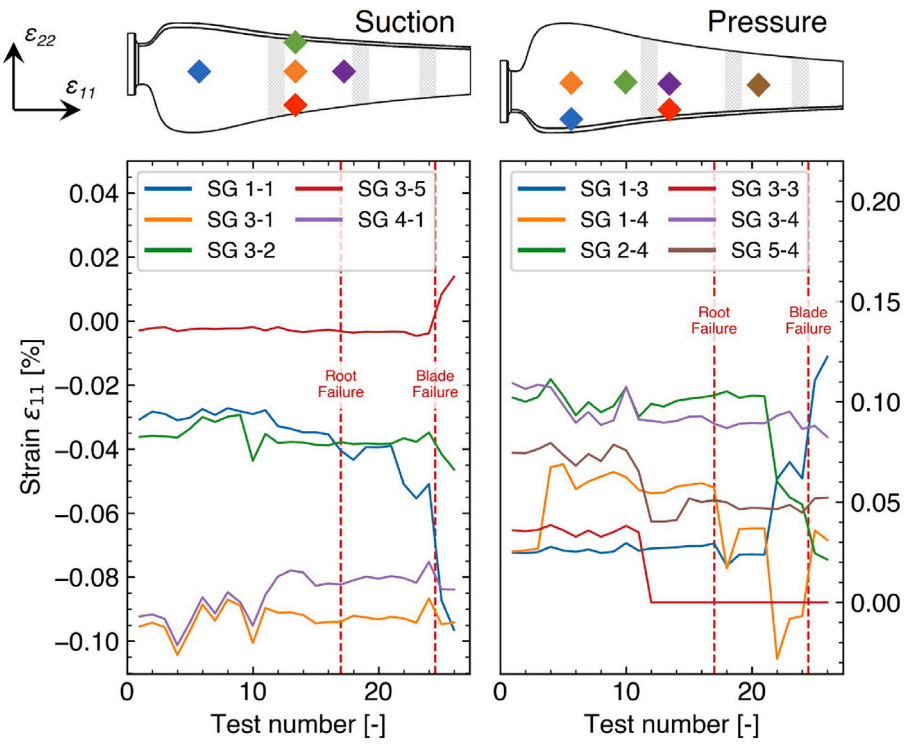

Fig. 12. Strain when a total load of 40 kN for all static tests is applied, for the suction side of the blade (left) and the pressure side of the blade (right).

disturbance in strain measurements. This region was found to absorb a substantial portion of the load, as load transfer to the suction side of the blade was no longer feasible.

A similar approach was applied in Fig. 13 to enable comparison of the strain gauges during fatigue testing. The troughs were selected over the peaks, as the fatigue tests did not share a consistent mean target load or amplitude. However, most tests maintained a similar minimum load of 15 kN. For each cycle, the trough value was identified and subsequently averaged across all cycles within a given test.

On the suction side of the blade, the strain gauges exhibited a gradual slope, indicative of damage progression once tests under test case "C" and beyond were conducted. This degradation in stiffness was further accelerated following the failure near the root, with the most pronounced damage observed in strain gauges located away from the trailing edge. Strain gauge 3–5, positioned nearest the trailing edge, registered only a slight increase in compressive strain, highlighting the important role of the rear spar to prevent damage initiation at the trailing edge reported in wind turbine blades [14,19,20].

On the pressure side of the blade, the consequences of failure event "B" were more distinctly captured in Fig. 13. The region between the root connection and the first actuator experienced a sudden reduction in load-bearing capability, as the skin was left free to move in the section where it was bonded to the iron root instead of the spar. This effect was not observed beyond the first actuator, where the skin remained bonded solely to the spar, although the trend continued at a reduced rate.

3.1. Skin–root interface failure

The first failure event occurred during static test 17 (test case C), in which we applied a total load of 660 kN at approximately 120 kN min^{-1} after the blade had accumulated roughly 86 256 cycles. Fig. 14 shows the load increment at four different stages behind the first actuator. Although no abrupt drop was recorded in the force or displacement measurements, the strain gauges captured a distinct redistribution of load along the blade. This behaviour is illustrated in Fig. 15, where the pressure side of the blade was more significantly affected than the suction side.

The red-dotted line denotes the exact moment at which the skin was de-bonded from the root connection. The de-bonding followed the contour of the skin around the root but did not complete a full circumferential separation, terminating upon reaching the top skin. This static skin–root debonding follows Zuo's observations of interface damage under high shear stresses [22], while the involvement of accumulated cycles before separation aligns with Hosseini-Toudeshky's findings of fatigue debonding at the same interface [10]. Gauges 1–4 and 2–4, located nearest the root, captured the distinctive redistribution that signalled the onset of failure.

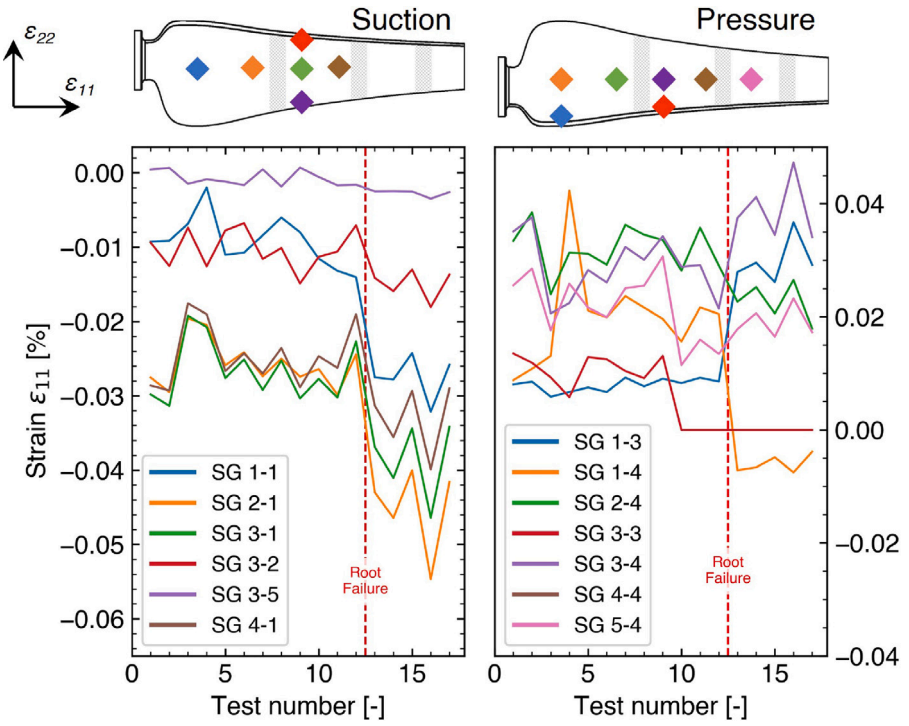

Fig. 13. Mean strain at the troughs of all fatigue tests, for the suction side of the blade (left) and the pressure side of the blade (right).

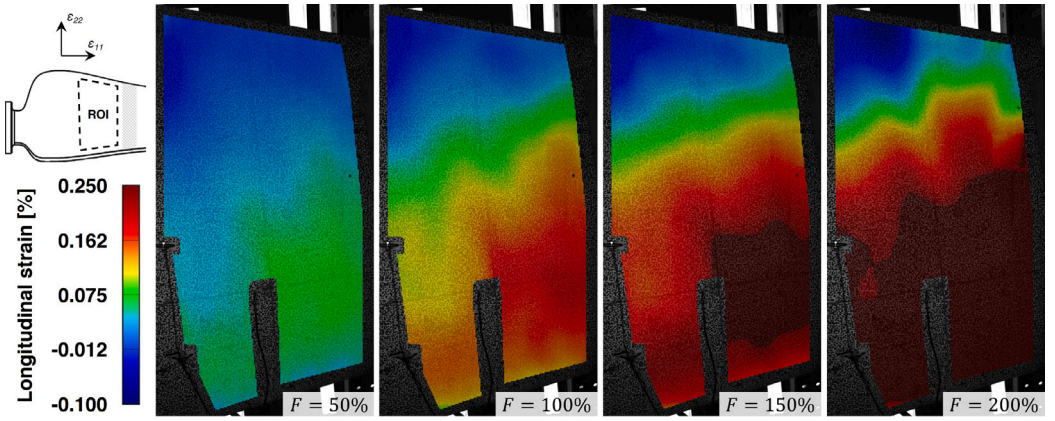

Fig. 14. DIC strain map for ROI 1 during static test 17 (failure event B), showing longitudinal strain at various load levels expressed as a percentage of the static design load (F = 283.29 kN).

Strain gauge 2–4 registered the maximum strain on the pressure side, reaching 0.481%, a value insufficient to indicate fibre breakage in this region. The ±45° strain gauges in the rosette configuration recorded maximum values of 0.177% and 0.175%, respectively, consistent with shear-dominated loading but still below critical failure thresholds. Strain gauge 2–4 was less affected than adjacent gauges near the failure feature. This behaviour can be attributed to the internal rib structure, as the first rib is located at 700 mm from the root and the rib at 1100 mm appears to effectively transfer load from the skin to the spar, establishing a load transfer boundary. Additionally, strain redistribution may have been influenced by local stiffness variations, residual manufacturing stresses, or partial adhesive failure prior to de-bonding.

A further look was taken surrounding the induced damage hole with its notches, as seen in Fig. 16. Two linear strain gauges were installed at the shadow-stress zones, one aligned in the direction of the root and the other in the direction of the tip. Two rosette strain gauges were installed near the high-stress zones, one adjacent to the notch towards the trailing edge and the other near the notch towards the leading edge. As expected, Fig. 16a shows the longitudinal strain close to the notches experiencing a higher strain

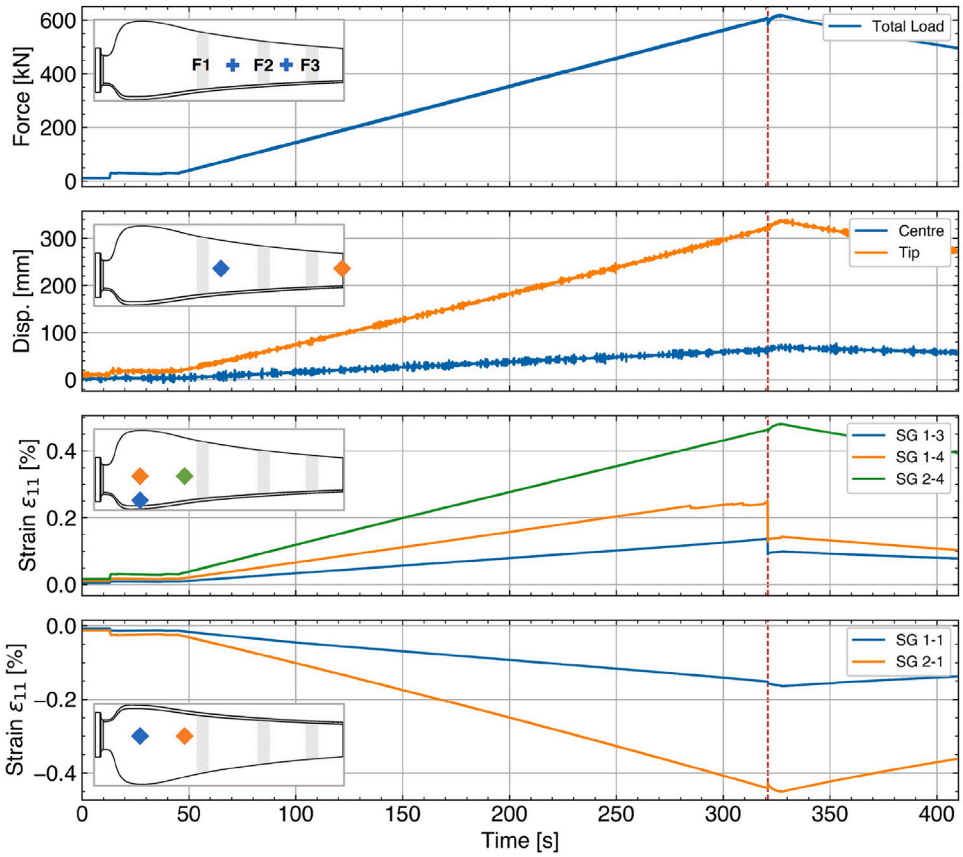

Fig. 15. Static test number 17 sensor readings from top to bottom: Load cells, displacements, longitudinal strain gauges at the pressure side of the blade, longitudinal strain gauges at the suction side of the blade.

value, with the strain gauge near the trailing edge reaching a maximum strain of 0.447%. Even at these high stress concentrations, the measured strain did not approach the ultimate strain for GFRP, which is about 2 per cent in epoxy matrix systems.

The resulting strain map from reaching the design load is shown in Fig. 16b. This distribution highlights the biaxial nature of the skin layup, with the prepregs oriented at +45 and −45 degrees. The average strain in this map is (0.1614 ± 0.1052)%, which increases in Fig. 16c to (0.3591 ± 0.1927)% immediately before failure. Fig. 16d shows a decrease in strain surrounding the hole after the skin de-bonded from the root, even though the applied load increased by an additional 15 kN. This observation further supports the assumption that the first 1100 mm of the bottom skin stops effectively transferring load to the root, with the load now redirected through the internal components.

The hole and its notches are no longer the regions of highest stress concentration. Although the blade is designed to carry load primarily through the spar, the initial load path unexpectedly relied on the skin's bond to the root, likely due to large discontinuities between the skin and adjoining components. To address this, test case "D" introduced notches to deliberately weaken the spar box and encourage additional damage before complete skin de-bonding at the root. Moreover, the observed strain redistribution indicates a progressive shift in load path driven by damage evolution, underscoring the internal structure (ribs and spar) in sustaining load transfer even after partial skin detachment. This structural integrity can be observed in Fig. 17, where the longitudinal strain shows minor changes on top of the spar box.

The observations translate directly to in-service blade behaviour and underscore the critical role of ribs in preserving short load-transfer paths. Fig. 18a shows a side view of the blade with its internal components. In the region close to the root, where no skin spar interface exists, the ribs alone carry the pressure load back to the root. If the skin–root interface fails, that load is rerouted to the nearest rib (Fig. 18b); without closely spaced ribs, stress concentrations form deeper along the blade where the spar and skin converge (Fig. 18c), placing excessive demand on the adhesive layer at that interface.

Prior work on rib design has mostly targeted weight reduction and frequency tuning in small wind blades [46] and in tidal blades [47]. In wind applications, rib placement influences bending modes, and optimisation of rib number and spacing with genetic algorithms reduces mass [48]. An optimisation study on large thermoplastic wind blades compared two parameters, the number of webs and the number of ribs, and found that a configuration with 35 ribs gave the lowest blade mass. It also reported that 5 mm ribs are required near the root to prevent buckling in both ribs and skins [49]. For context, the ribs in our blade were 6 mm thick.

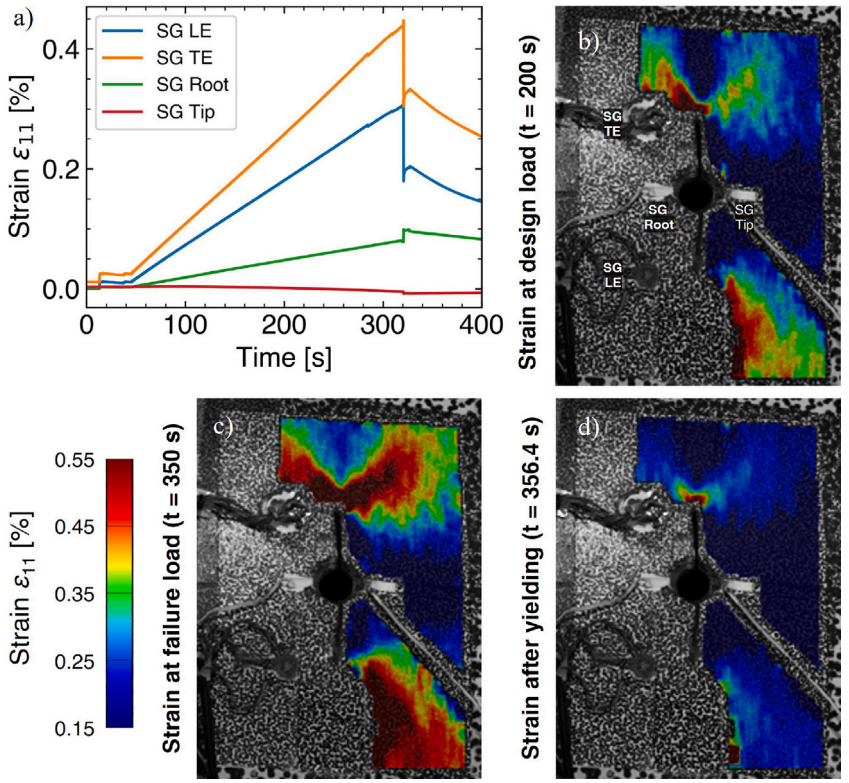

Fig. 16. Hole analysis during root failure: (a) Strain gauges surrounding the hole; (b) Strain map at the design static load (283.29 kN); (c) Strain map at failure event; (d) Strain map of the structural response after failure event.

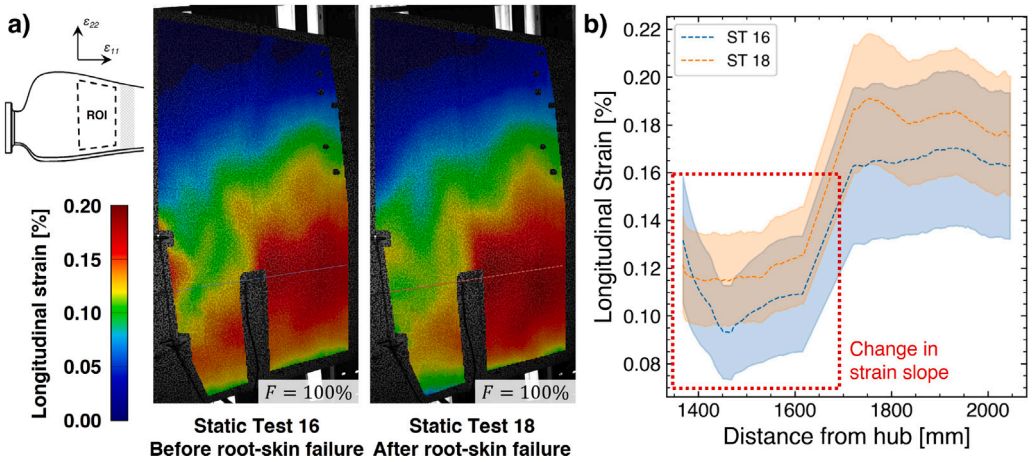

Fig. 17. Longitudinal strain comparison between static tests before and after the root-skin failure: (a) Strain maps at the ROI 1; (b) Strain along the neutral axis of the blade.

Failure analysis has shown that ribs can increase strength under flapwise loading by up to 30% [17], and a separate study reduced rib count from 21 to 7 on a 4 m blade by using connecting rods while maintaining performance [50].

Building on these insights, our study recommends a tidal specific optimisation that reflects shear dominated loading and the absence of a skin spar bond in the proximal region. The priority variables are rib spacing that could be denser near the root, geometry transitions, and regions without a skin spar interface; a variable rib thickness; rib material and lay up selection, including hybrid laminates; and rib flange length and bond detailing to control peel and shear at the skin and spar interfaces. We also recommend quality controls to minimise voids at rib to skin and rib to spar bonds.

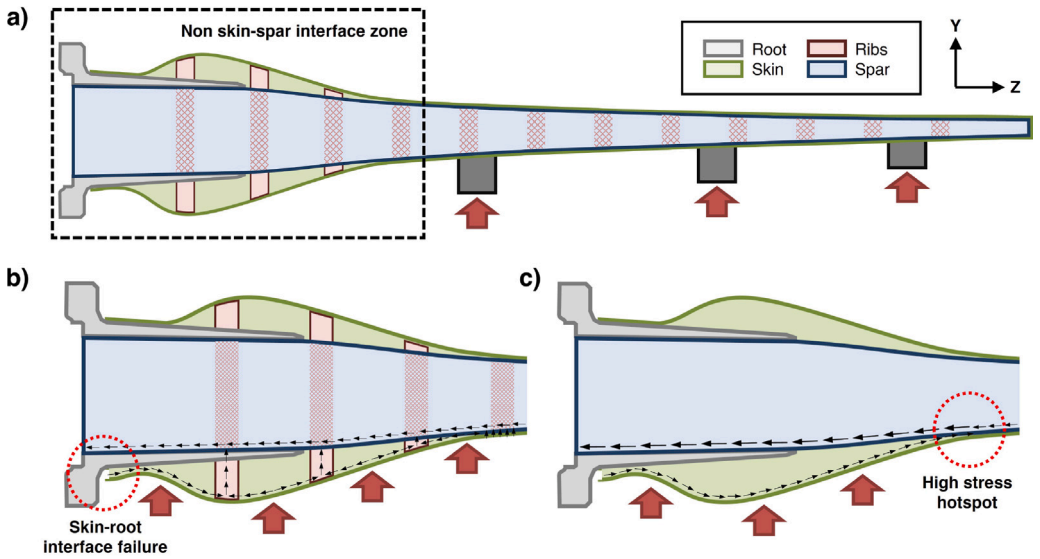

Fig. 18. Load routing diagram of the blade and its internal components: (a) Side view illustrating saddle load application; (b) Operational load path after skin–root debonding with closely spaced ribs; (c) Operational load path after skin–root debonding when ribs are absent.

3.2. Skin-skin interface failure

The final failure event shown in Fig. 19a occurred under test case "D" conditions, with a highly weakened spar box. The length of each notch extended past the location of the shear webs, effectively creating vertical notches on these components, each with a length of 100 mm. Surface micro-cracks were observed propagating in the +45 and −45 degree directions from both crack tips on the skin surface. Strain gauges also started to show a slow increase in their readings, but further inspection of the blade revealed no visible signs of major damage.

The final test was fatigue test number 17, which aimed to load the blade for 20 000 cycles, but it only reached 2432 cycles before complete failure was observed. The mean load for this test was 47.5 kN per actuator with an amplitude of 27.5 kN. A closer examination indicated that the final failure was caused by debonding between the top and bottom layups of the skin, which was further corroborated by a simplified schematic of the section view of the blade in Fig. 19b. A closer look at the gap between these two layups in Fig. 19c shows a clean cut, with the plies within the skin showing no major damage. The adhesive exhibited brittle behaviour, as it completely de bonded from both layups and shattered along the length of the delamination zone. This final failure event can be explained by the progressive fatigue degradation of the adhesive bond which, after repeated loading cycles, weakened to the point of catastrophic failure. The presence of surface micro cracks and strain gauge readings pointing to increased local strain before final failure further supports the theory of progressive damage accumulation common in adhesive bond failures under cyclic loading conditions.

The failure feature initiated at the complex geometry transition from the circular root to the largest airfoil, matching Zuo's observations of interface debonding locations under high shear [22]. Although this location lies closer to the leading edge region noted by Bir [12], the debonding occurred on the pressure side rather than the suction side reported by Lee and Overgaard [25,26], likely due to the artificial damage (drilled hole and notches) being introduced there. The large drop of load bearing capacity in the sparbox makes it unclear whether damage would have arisen naturally at this site without a considerable level of manufacturing defects.

Fig. 20 shows data from sensors during the last cycles before the blade failed. The average maximum load applied at the peak of the cycles was 75 kN per actuator before suddenly increasing to 102 kN per actuator. It can also be observed that the strain gauge on the notch closer to the leading edge read a higher strain value during the cycles than the strain gauge located closer to the trailing edge. This difference swaps once de-bonding in the leading edge occurs, effectively transferring some of the load-bearing capacity to the rear spar. This phenomenon decreases along the span of the blade as the failure feature spread only to a distance of 2.42 m from the root.

Strain gauge 1–3 shows the biggest jump during failure amongst the strain gauges located on the pressure side of the blade, between the root connection and the first saddle. The reading drops to a minimum value of 0.101% and reaches a maximum value of 0.213%, despite the load decreasing to an average of (66.72 ± 3.98) kN per actuator. Strain gauge 1–4 shows a change from compression back to tension in strain given that this is located in a shadow-stress zone between the detached root and the drilled hole. On the other hand, the suction side of the blade shows less impact in its load distribution. Past the first saddle, strain variation is lower with strain gauge 3–2 reading a difference in strain of only 0.083% between the maximum and minimum value during the failure event. Strain gauge 2–1 shows the biggest change in strain on the suction side of the blade, with a difference of 0.299% in

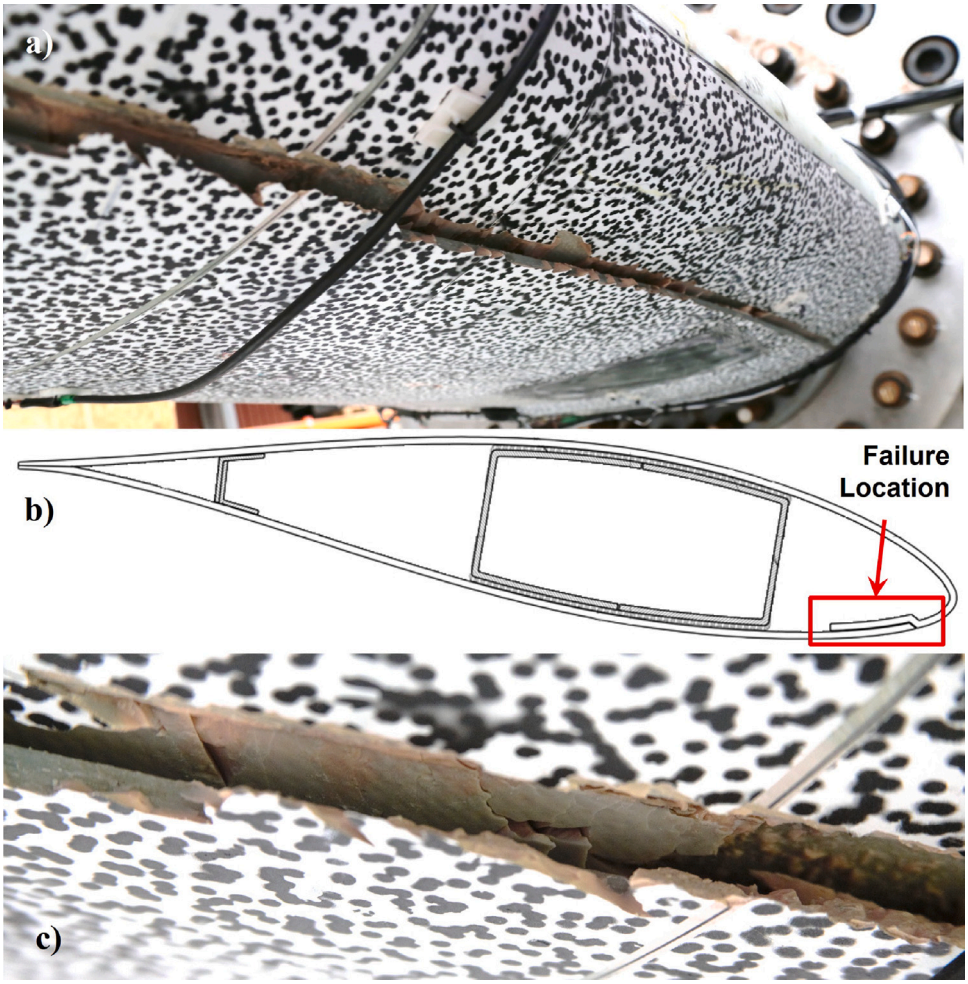

Fig. 19. Final blade failure: (a) General view; (b) Failure feature in a section view diagram; (c) Detailed view along the skin seam of the blade.

strain between the onset of failure and the maximum strain reached. These readings suggest that de-bonding started in the region between the drilled hole and the first saddle.

The +45 and −45 readings in strain gauge 2–1 show strain values along the fibres below the failure strain required at −0.2% and −0.228%, respectively. This is consistent with the progressive nature of delamination in composite structures, where strain concentration at critical points (such as near notches or drilled holes) accelerates the local damage, leading to the redistribution of loads to other parts of the structure. The observed strain values in the region between the drilled hole and the first saddle support the theory of localised delamination propagation before a full structural failure, which is typical in fatigue testing of composite materials.

The steady increase in strain measurements was observed in most strain gauges during this test, in contrast to previous tests where peak values remained stable even after 20 000 cycles had been run continuously. For instance, Fig. 21(a) shows one of the strain gauges closest to the failure feature. During the test, the strain at the peak of each cycle was observed to increase gradually. The introduction of a trend line indicates that the strain increased at a rate of 0.00262% per 1000 cycles. This trend diminished as the distance from the failure location increased, with strain gauge 3–2 in Fig. 21(b) showing a strain rate of 0.000177% or 1.777 $\mu m\ m^{-1}$ per 1000 cycles. The progression of damage throughout the test could not be detected by the load cells, as the system operated under load control. However, the displacement sensors recorded a steady increase, which was particularly magnified at the tip of the blade. This increase is shown in Fig. 21(c), where the strain rate is 1.45 mm per 1000 cycles.

The DIC analysis of this fatigue test focused on the regions of interest surrounding the notch tips. Fig. 22 presents a direct comparison of these high-stress zones between the first cycle and the cycles close to the failure event. It was observed that cracks continued to grow from the notch tips in both the +45 and −45 degree directions, propagating along the fibres and exhibiting significant matrix cracking. The notch closer to the trailing edge exhibited a higher number of micro-cracks than the notch near the leading edge. This observation is corroborated in the first cycle, where the trailing edge notch region showed an average strain of (0.375 ± 0.335)%, which is lower than the average strain of (0.539 ± 0.321)% in the leading edge notch region. This difference

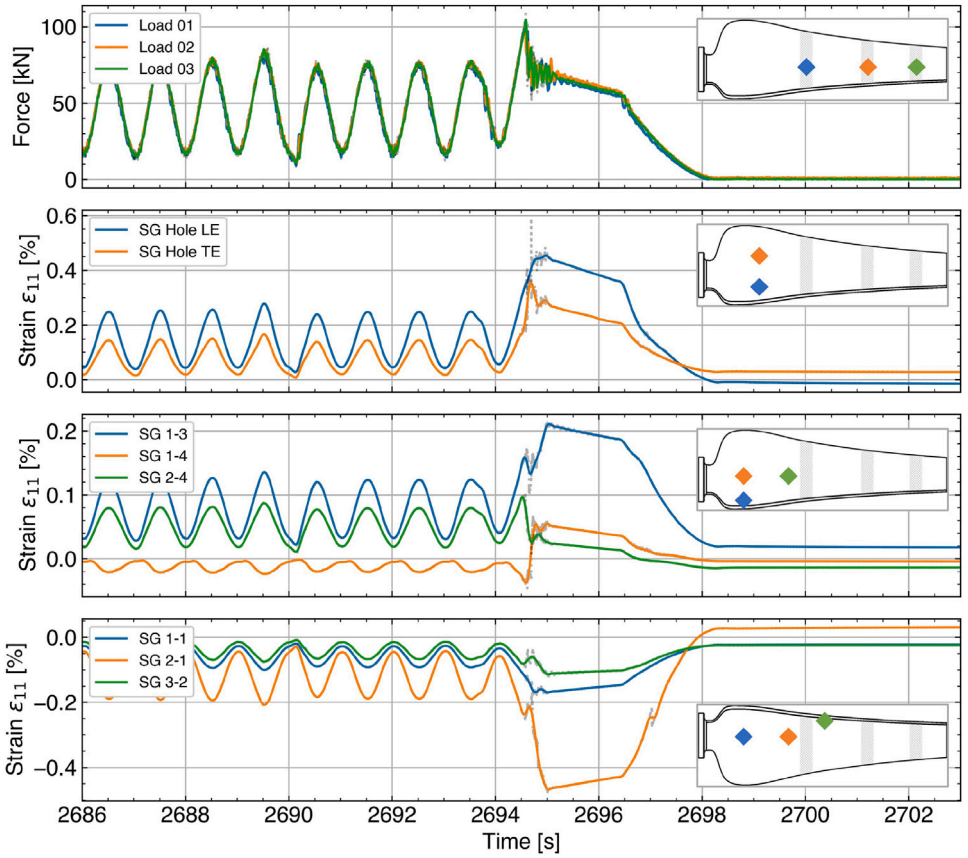

Fig. 20. Last 10 cycles of the last fatigue test before ultimate failure. From top to bottom: Load applied per actuator, strain gauge measurements close to the hole notches, strain gauge measurements at the pressure side of the blade, strain gauge measurements at the suction side of the blade.

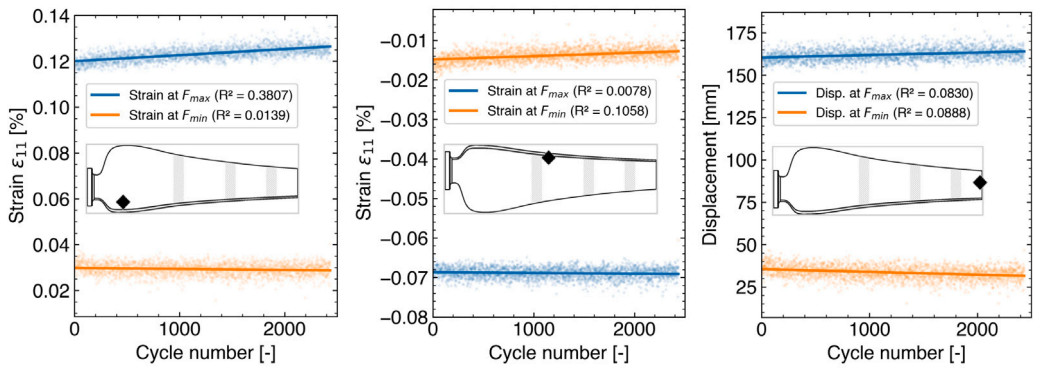

(a) Strain gauge 1-3. (b) Strain gauge 3-2. (c) Displacement at the tip.

Fig. 21. Peaks and troughs during the entire fatigue test that led to final failure.

shifted during the course of the fatigue test, as the statistics indicated a higher average strain of (0.421 ± 0.401)% in the trailing edge notch region compared to the leading edge region, which showed (0.194 ± 0.145)%. Finally, after the blade failure, the DIC analysis revealed that the leading edge notch transitioned into a shadow-stress zone, with the average strain in that region dropping to (−0.028 ± 4.131)%, exhibiting a high standard deviation that suggests rigid body motion was considered as strain. In contrast, the region surrounding the trailing edge notch largely remained above 0.1% strain.

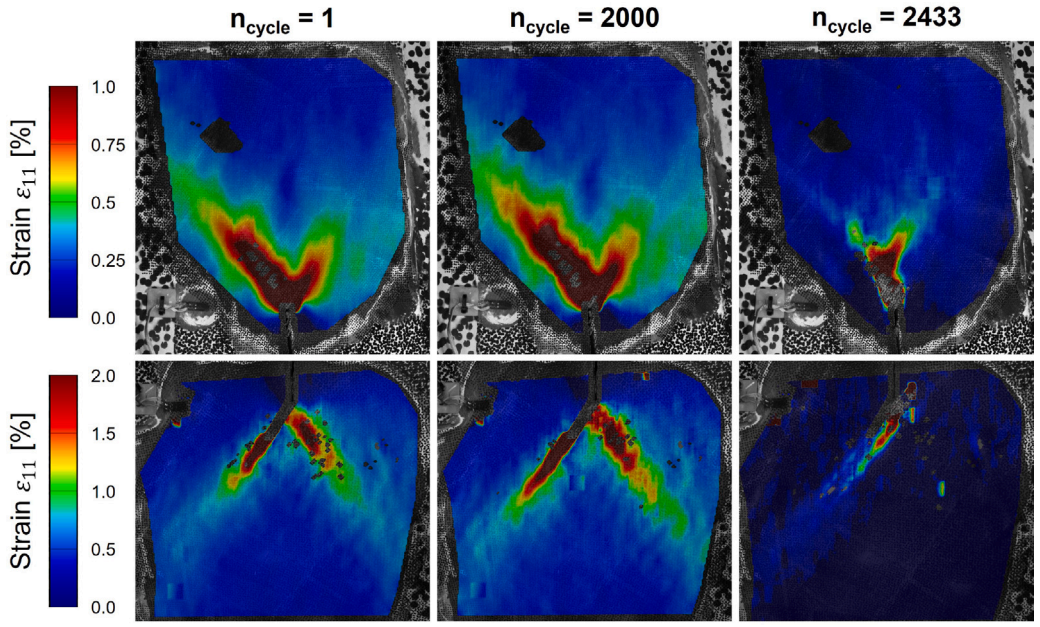

Fig. 22. DIC strain maps surrounding the hole notch close to the trailing edge (top) and close to the leading edge (bottom), at different cycles during the last fatigue test.

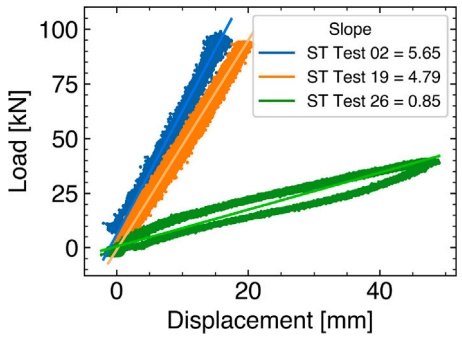

Fig. 23. Load vs. displacement comparison in the first actuator, between reference static test and static tests after failure events.

3.3. Post-failure analysis

Two additional static tests were attempted after the tidal blade failed during the last fatigue test, which was caused by the de-bonding of the top and bottom skin layups. The first static test aimed to reach 100% of the static design load. However, failure continued to propagate as the de-bonding extended along the span of the blade. The test was terminated at a total load of 166.65 kN (68% of the static design load) when the load sensor registered abrupt drops and the third actuator piston neared its maximum stroke.

A final static test was performed at a lower target load of 42.4 % of the static design load, corresponding to a total load of 120 kN applied to the blade. The blade showed a lower level of damage progression and finally stabilised after holding the target load for 2 min. Residual strength could be quantified in accordance with the DNV GL ST-0164 standard [43], comparing the global stiffness of the blade before and after failure (see Fig. 23). Static test number 2 serves as a good reference before any damage was introduced to the blade, running under test case "A" conditions. Static test number 19 was the first static test conducted at full design static load after the skin–root interface failure. The trend line of displacement against load shows a slight decrease in the slope (stiffness) after the first failure event. This effect could be minimised by the role of the ribs in the load transfer within the structure, as they effectively create short paths to channel the surface pressure directly to the spar.

The stiffness drastically decreased for the final static test from 4.79 kN mm to 0.85 kN mm. The blade shows an overall 85% decrease in stiffness, which would not comply with the current testing certification frameworks. The last static test also showed a similar behaviour to a hysteresis loop; however, this is the result of further damage progression in the blade as the load was ramped up.

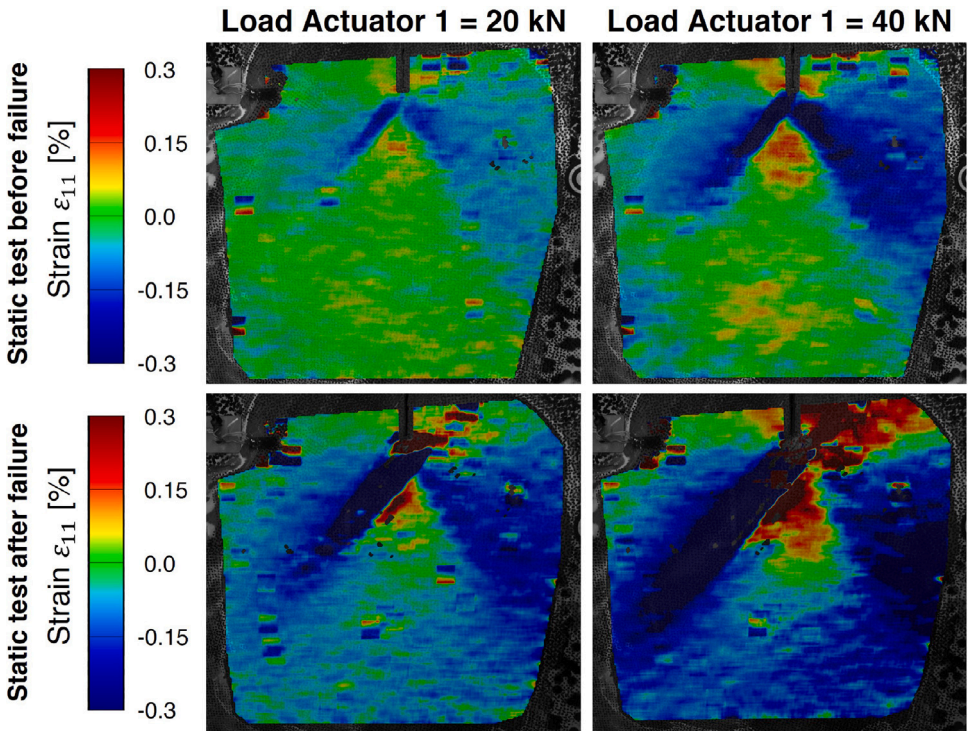

Fig. 24. DIC comparison of the region close to the leading edge notch between static tests before and after the fatigue test where final failure occurred.

Although the blade was artificially weakened due to the different test conditions, their contributions were minimal to the change in displacement. Consequently, the observed increase in displacement can be attributed primarily to the failure events. In parallel, we detected a drop in the first natural frequency, from 18.01 Hz to 14.69 Hz; the corresponding FFT and PSD modal analyses for one accelerometer are shown in Figure S.1 of Supplementary Section S.2. Performing modal tests during fatigue loading can therefore serve as a useful global stiffness indicator when damage is not evident from local instrumentation.

Another comparison was made between the static tests conducted before and after the critical fatigue test where the final failure occurred. Static test number 24 was performed before the last fatigue test and aimed to apply 68.8% of the static design load. The comparison was made at 20 kN and 40 kN per actuator, as the last static test reached a maximum applied load equal to 42.4% of the static design load. The DIC strain map of these comparisons is shown in Fig. 24. The fibres in the +45 degree direction exhibited the most damage, with matrix cracking dominating most of the region. The strain map after failure shows a larger area where compression is taking place compared to the test before failure. On average, the strain in this region before failure was (-0.0635 ± 0.108)%, compared to a strain of (-0.102 ± 0.205)% after failure.

A qualitative assessment was conducted after the last static test to understand the extent and nature of the final failure feature. A portion of the top skin was extracted, as it had completely detached from the bottom skin in the section between the root and the first saddle. Fig. 25a shows the skin overlap section, where it can be observed that the adhesive de-bonded in a clean manner, indicating subpar adhesive performance. Samples were extracted from the exact bond line where the top skin ends before encountering the bottom skin. Two types of samples were extracted at several locations along the length of the blade. Fig. 25b shows a sample extracted at a failed location where the top skin is no longer attached to the bottom skin. In contrast, Fig. 25c shows a sample from the same bond line at a location where the adhesive had not failed, and the top and bottom skins were still securely attached. The number of samples extracted was limited by the requirement to return the blade to the lending organisation, making full adhesive-layer removal impractical.

The extracted samples (5 damaged and 3 undamaged) were then examined using a scanning electron microscope (SEM), where surface images were captured with an accelerating voltage of 10 kV, an average working distance of 7.2 mm, and a backscattered electron SEM imaging mode. The samples from the undamaged bond line showed a generally stable level of integrity between plies, as shown in the top images of Fig. 26. However, the thick adhesive bonding the top and bottom skin exhibited through-thickness cracks, with half of the samples showing these cracks extending entirely through the bonding layer. This indicates that the adhesive was experiencing progressive damage, which could later lead to the complete de-bonding of the two skin layups. It was also noted that the thickness of the bond layer varied across the length of the blade, which might contribute to the heterogeneity of the stiffness in this bond line. On the other hand, the bottom images of Fig. 26 show samples from the failure location, where signs of delamination between the skin plies were observed. The length of this separation ranged from 4.5 mm to 24 mm, but it was only

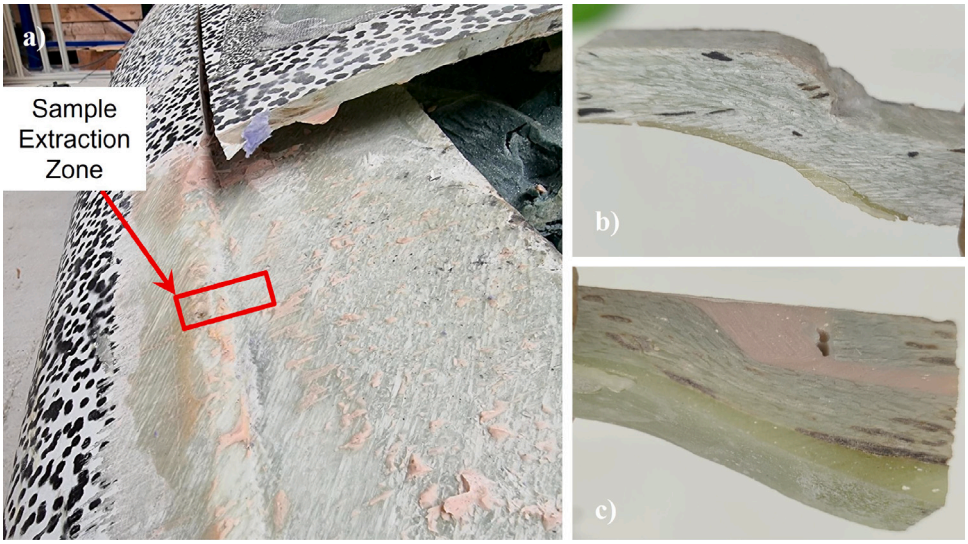

Fig. 25. Sample extraction at skin seam, (a) Full failure location extraction location; (b) Sample extracted at failure location; (c) Sample extracted at undamaged location.

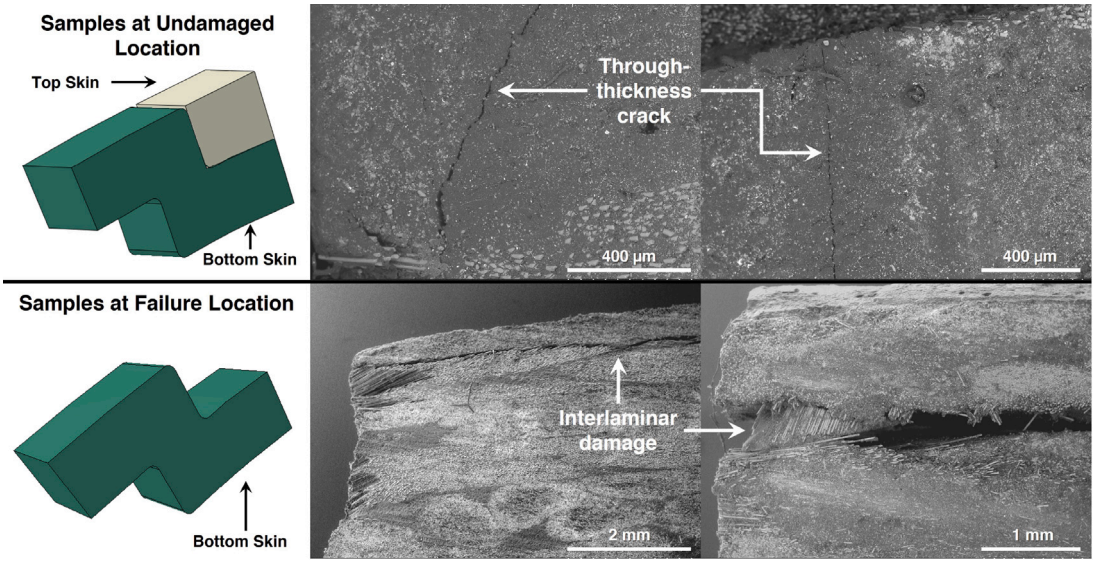

Fig. 26. Microscope images from different samples extracted at the skin seam along the blade.

present in the first ply of each sample, agreeing with near-surface delamination caused by buckling in [18]. It could be assumed that delamination was caused by buckling, rather than developing independently during the fatigue tests. This further emphasises that the bond between the plies is stronger than the adhesive holding the components together, making the bonding material one of the most critical components of the blade's structure.

As mentioned in the previous section, the rear spar began to take a considerable portion of the load after the bond line had failed. For this reason, three cylindrical samples were taken at evenly spaced locations along the length of the blade and 200 mm from the trailing edge. Fig. 27a shows a microscope image of the GFRP plies laid up in the rear spar. In all the samples, the rear spar plies exhibited no signs of interlaminar or intralaminar damage. It was observed that the thickness of the bond layer between the skin and the spar is relatively large compared to these components, with Fig. 27b showing one of the samples where the bond layer is twice the thickness of one of the skin plies. This increased thickness raises the likelihood of large voids if not properly curated during the blade's assembly, which was observed at various locations across the blade. Smaller voids were found throughout the thickness of both the rear spar layup and the skin layup. The dimensions of one such void are shown in Figs. 27c and 27d, where at its thickest point, it accounts for 31% of the GFRP ply cured thickness.

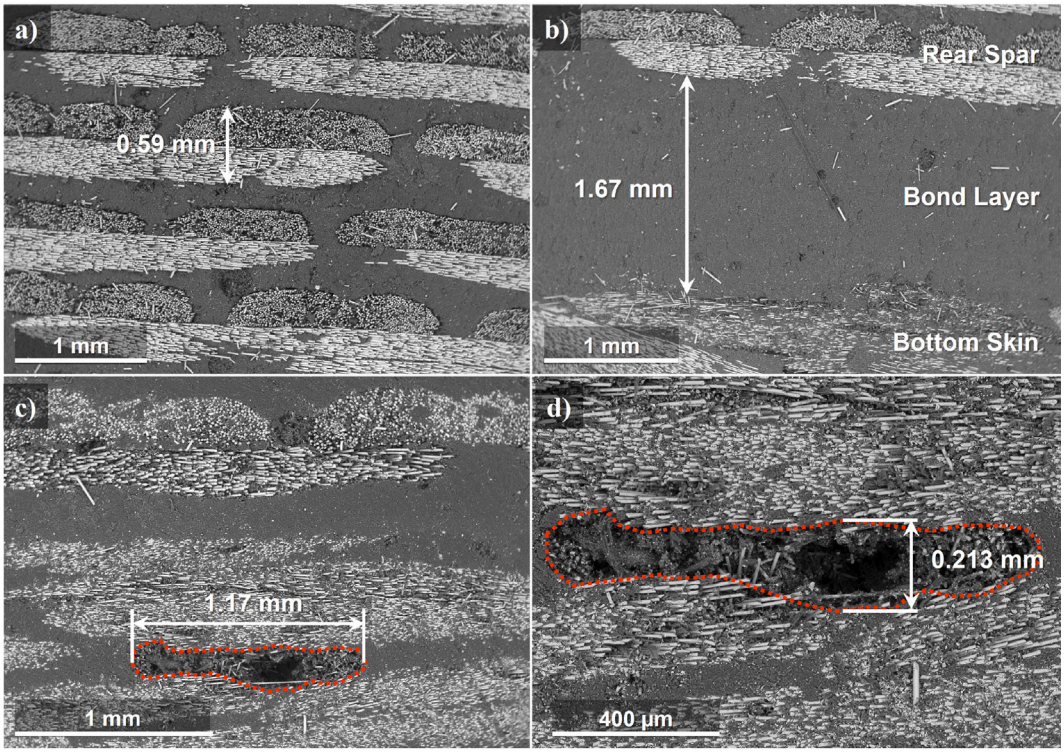

Fig. 27. Microscope images from the trailing edge section: (a) undamaged individual biaxial GFRP plies in the rear spar; (b) interface zone between the bottom skin and the rear spar; (c) manufacturing defects in the bottom skin; (d) void between individual GFRP plies.

Prior work highlights adhesives as a critical concern for blade reliability, especially in the later years of service life. Voids arising from fast cure schedules and non-uniform heat distribution can accelerate adhesive fatigue [51]. Reviews of thin and thick composite joints show there is no single criterion for selecting bondline thickness because it depends on the adherend materials and their surface preparation [52]. For thicknesses above about 3 mm, damage mechanisms are less well understood since a plastic zone ahead of the crack tip can dominate crack growth; fillet joints can even fail differently across their width, with one side showing cohesive adhesive failure and the other side delaminating the CFRP [53]. Thickness also trades fracture toughness against shear response: increasing thickness may raise fracture toughness but can reduce shear stiffness and strength [54]. Architected joints with crack arrest features can improve damage tolerance, although these results are mainly for mode I loading [55]. Our tidal blade interfaces are governed primarily by mode II and mode III shear, and studies on single lap aluminium–epoxy joints report decreasing strength with increasing adhesive thickness under mode II conditions [56].

Based on these insights and our findings, we recommend tidal specific studies that focus on bondline thickness and void control. This includes parametric tests on composite to composite and composite to root joints under mode II and mode III fatigue, with bondline thickness and void density as primary variables, alongside surface preparation and cure schedules. Assembly processes can also be improved by achieving a uniform thickness using calibrated spacers and well-defined fillets to lower peel stresses. Lastly, adhesive layers should be instrumented to monitor performance and enable early detection of damage. This shift in focus from bulk material strength to the behaviour of adhesive interfaces is essential for durable tidal blade design.

The largest voids were found after taking the skin off at different locations across the blade. Fig. 28 illustrates the dimensions of these voids. As their size increases, so does the number of discontinuities, and thus the number of high–stress concentration points. Such voids were found at various locations on the blade, including the interface between the skin and the spar. This observation aligns with Corren's report on the large quantity of voids in internal component joints [32]. Overall, manufacturing defects appear to play a significant role in each component's ability to transfer loads effectively to the spar box. Mapping the void distribution in a blade prior to testing could guide more strategic instrumentation placements towards areas prone to failure.

Lastly, we introduce a global stiffness metric to capture the blade's damage progression over the entire experimental phase. We selected the tip displacement sensor as a reference, since it remained largely unaffected by changes in saddle material, actuator alignment, loading conditions, and individual failure events. Global stiffness is therefore defined as the total load from all three actuators divided by the tip displacement. Fig. 29 plots this metric over 97 000 cycles experienced by the blade, revealing a steady decline in stiffness that accelerates once artificial defects are introduced. This trend complements the observed reduction in natural frequency and underscores the importance of studying the integrity of adhesive interfaces layers over bulk material strength analyses.

Fig. 28. Adhesive voids (highlighted with a red dashed line) in the interface between the filling foam and the skin layup.

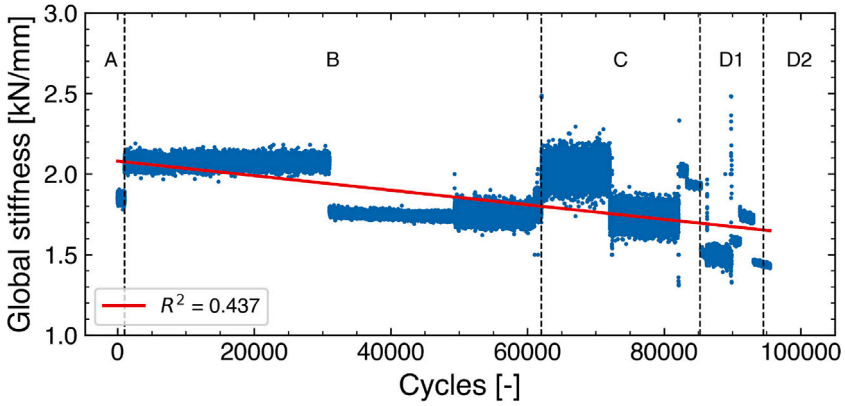

Fig. 29. Global stiffness metric against number of cycles, throughout the different test conditions.

4. Conclusions

This study examined the failure mechanisms of a 5.25 m tidal turbine blade under static and fatigue loading. The results underscore the extreme shear demands and associated challenges for test rigs when evaluating tidal blades compared to conventional wind turbine blades. Three primary failure events were identified: saddle-fixture failure, root–skin interface debonding, and pressure–suction skin debonding; which lead to the following key insights:

- **Local vs. global stiffness**: Although artificial defects and matrix micro-cracks reduced local stiffness, global blade stiffness remained largely unchanged, suggesting that short-term impacts (e.g., debris strikes) may not immediately compromise performance.
- **Experimental-setup flexibility**: The first failure occurred in the saddle fixtures rather than the blade, emphasising the need for robust, adaptable test rigs capable of delivering the extreme loads required to cause failure in tidal blades.
- **Adhesive-interface vulnerability**: Bondline failures between composite layers and between composite and metal components govern the blade's collapse, highlighting the need for dedicated fatigue life and damage progression studies on these joints under shear-dominated loading conditions.

- **Redundancy of internal ribs and rear spars**: Internal ribs and the rear spar successfully reroute loads after skin–root debonding, delaying catastrophic failure. A systematic parametric analysis of their spacing, material and lay-up is therefore essential to optimise blade resilience.
- **Instrumentation requirements**: Capturing through-thickness strain gradients and potential neutral axis shifts will require placing sensors on adhesive layers, adding gauges on shear webs, and using side-view digital image correlation to identify critical strain gradients.
- **Manufacturing quality control**: Large voids at skin-to-structure interfaces act as high-stress concentrators; minimising these defects through enhanced lamination processes and non-destructive inspection is critical to improving structural integrity.

Addressing these areas will be vital for enhancing the reliability, maintainability and certification prospects of future tidal turbine blades. Further work could also develop and validate finite element models to optimise adhesive joint properties and interface performance.

CRediT authorship contribution statement

Miguel A. Valdivia-Camacho: Writing – original draft, Visualization, Validation, Software, Methodology, Investigation, Formal analysis, Data curation, Conceptualization. **Fergus Cuthill:** Writing – review & editing, Software, Resources, Methodology, Investigation, Data curation. **Edward D. McCarthy:** Writing – review & editing, Resources, Project administration. **Sergio Lopez Dubon:** Writing – review & editing, Supervision, Resources, Methodology, Data curation. **Conchúr M. Ó Brádaigh:** Writing – review & editing, Supervision, Resources, Project administration, Methodology, Funding acquisition, Conceptualization. **Parvez Alam:** Writing – review & editing, Supervision, Resources, Methodology, Conceptualization.

Declaration of competing interest

The authors declare that they have no known competing financial interests or personal relationships that could have appeared to influence the work reported in this paper.

Acknowledgements

M.A. Valdivia-Camacho: This research was supported by the Wind & Marine Energy Systems & Structures (WAMESS) CDT under the Engineering and Physical Sciences Research Council, United Kingdom grant agreement EP/S023801/1.

Appendix A. Supplementary data

Supplementary material related to this article can be found online at https://doi.org/10.1016/j.engfailanal.2025.110076.

Data availability

Data will be made available on request.

References

[1] Z. Maksumic, UK awards six tidal stream projects with contracts for difference in allocation round 6, Offshore Energy (2024).
[2] S. Walker, P. Thies, A review of component and system reliability in tidal turbine deployments, Renew. Sustain. Energy Rev. 151 (2021) 111495, http://dx.doi.org/10.1016/j.rser.2021.111495.
[3] W. Li, H. Zhou, H. Liu, Y. Lin, Q. Xu, Review on the blade design technologies of tidal current turbine, Renew. Sustain. Energy Rev. 63 (2016) 414–422, http://dx.doi.org/10.1016/j.rser.2016.05.017.
[4] M. Nachtane, M. Tarfaoui, I. Goda, M. Rouway, A review on the technologies, design considerations and numerical models of tidal current turbines, Renew. Energy 157 (2020) 1274–1288, http://dx.doi.org/10.1016/J.RENENE.2020.04.155.
[5] F. Zhu, L. Ding, B. Huang, M. Bao, J. Liu, Blade design and optimization of a horizontal axis tidal turbine, Ocean Eng. 195 (2020) 106652, http://dx.doi.org/10.1016/j.oceaneng.2019.106652.
[6] S. Astariz, A. Vazquez, G. Iglesias, Evaluation and comparison of the levelized cost of tidal, wave, and offshore wind energy, J. Renew. Sustain. Energy 7 (2015) 053112, http://dx.doi.org/10.1063/1.4932154.
[7] D. Grogan, S. Leen, C. Kennedy, C. Ó Brádaigh, Design of composite tidal turbine blades, Renew. Energy 57 (2013) 151–162, http://dx.doi.org/10.1016/j.renene.2013.01.021.
[8] P. Davies, G. Germain, B. Gaurier, A. Boisseau, D. Perreux, Evaluation of the durability of composite tidal turbine blades, Philos. Trans. R. Soc. A: Math. Phys. Eng. Sci. 371 (2013) 20120187, http://dx.doi.org/10.1098/rsta.2012.0187.
[9] P. Alam, C. Robert, C. Ó Brádaigh, Tidal turbine blade composites - a review on the effects of hygrothermal aging on the properties of CFRP, Compos. Part B: Eng. 149 (2018) 248–259, http://dx.doi.org/10.1016/j.compositesb.2018.05.003.
[10] H. Hosseini-Toudeshky, M. Jahanmardi, M. Goodarzi, Progressive debonding analysis of composite blade root joint of wind turbines under fatigue loading, Compos. Struct. 120 (2015) 417–427, http://dx.doi.org/10.1016/j.compstruct.2014.10.025.
[11] N. Asseff, H. Mahfuz, Design and finite element analysis of an ocean current turbine blade, OCEANS 2009 (2009) 1–6, http://dx.doi.org/10.23919/OCEANS.2009.5422135.
[12] G. Bir, M. Lawson, Y. Li, Structural design of a horizontal-axis tidal current turbine composite blade, in: ASME 2011 30th International Conference on Ocean, Offshore and Arctic Engineering, 2011, pp. 797–808, http://dx.doi.org/10.1115/OMAE2011-50063.

[13] E. Fagan, C. Kennedy, S. Leen, J. Goggins, Damage mechanics based design methodology for tidal current turbine composite blades, Renew. Energy 97 (2016) 358–372, http://dx.doi.org/10.1016/j.renene.2016.05.093.
[14] X. Chen, W. Zhao, X. Zhao, J. Xu, Preliminary failure investigation of a 52.3 m glass/epoxy composite wind turbine blade, Eng. Fail. Anal. 44 (2014) 345–350, http://dx.doi.org/10.1016/j.engfailanal.2014.05.024.
[15] X. Chen, M. Eder, A critical review of damage and failure of composite wind turbine blade structures, IOP Conf. Ser.: Mater. Sci. Eng. 942 (2020) 012001, http://dx.doi.org/10.1088/1757-899X/942/1/012001.
[16] X. Chen, S. Semenov, M. McGugan, S. Hjelm Madsen, S. Cem Yeniceli, P. Berring, K. Branner, Fatigue testing of a 14.3 m composite blade embedded with artificial defects – damage growth and structural health monitoring, Compos. Part A: Appl. Sci. Manuf. 140 (2021) 106189, http://dx.doi.org/10.1016/j.compositesa.2020.106189.
[17] F. Jensen, B. Falzon, J. Ankersen, H. Stang, Structural testing and numerical simulation of a 34 m composite wind turbine blade, Compos. Struct. 76 (2006) 52–61, http://dx.doi.org/10.1016/j.compstruct.2006.06.008.
[18] P. Haselbach, R. Bitsche, K. Branner, The effect of delaminations on local buckling in wind turbine blades, Renew. Energy 85 (2016) 295–305, http://dx.doi.org/10.1016/j.renene.2015.06.053.
[19] H. Lee, J. Park, Static test until structural collapse after fatigue testing of a full-scale wind turbine blade, Compos. Struct. 136 (2016) 251–257, http://dx.doi.org/10.1016/j.compstruct.2015.10.007.
[20] V. Raman, M. Drissi-Habti, L. Guillaumat, A. Khadhour, Numerical simulation analysis as a tool to identify areas of weakness in a turbine wind-blade and solutions for their reinforcement, Compos. Part B: Eng. 103 (2016) 23–39, http://dx.doi.org/10.1016/j.compositesb.2016.07.018.
[21] R. Rafiee, M. Hashemi-Taheri, Failure analysis of a composite wind turbine blade at the adhesive joint of the trailing edge, Eng. Fail. Anal. 121 (2021) 105148, http://dx.doi.org/10.1016/j.engfailanal.2020.105148.
[22] Y. Zuo, J. Montesano, C. Singh, Assessing progressive failure in long wind turbine blades under quasi-static and cyclic loads, Renew. Energy 119 (2018) 754–766, http://dx.doi.org/10.1016/j.renene.2017.10.103.
[23] J. Yang, C. Peng, J. Xiao, J. Zeng, S. Xing, J. Jin, H. Deng, Structural investigation of composite wind turbine blade considering structural collapse in full-scale static tests, Compos. Struct. 97 (2013) 15–29, http://dx.doi.org/10.1016/j.compstruct.2012.10.055.
[24] L. Zhang, Y. Guo, J. Wang, X. Huang, X. Wei, W. Liu, Structural failure test of a 52.5 m wind turbine blade under combined loading, Eng. Fail. Anal. 103 (2019) 286–293, http://dx.doi.org/10.1016/j.engfailanal.2019.04.069.
[25] H. Lee, M. Kang, J. Park, Fatigue failure of a composite wind turbine blade at its root end, Compos. Struct. 133 (2015) 878–885, http://dx.doi.org/10.1016/j.compstruct.2015.08.010.
[26] L. Overgaard, E. Lund, Structural collapse of a wind turbine blade. Part b: Progressive interlaminar failure models, Compos. Part A: Appl. Sci. Manuf. 41 (2010) 271–283, http://dx.doi.org/10.1016/j.compositesa.2009.10.012.
[27] H. Ullah, B. Ullah, V. Silberschmidt, Structural integrity analysis and damage assessment of a long composite wind turbine blade under extreme loading, Compos. Struct. 246 (2020) 112426, http://dx.doi.org/10.1016/j.compstruct.2020.112426.
[28] H. Ullah, K. Alam, M. Iqbal, A. Husain, V. Silberschmidt, Simulation of buckling-driven progressive damage in composite wind turbine blade under extreme wind loads, Eng. Fail. Anal. 140 (2022) 106574, http://dx.doi.org/10.1016/j.engfailanal.2022.106574.
[29] J. Rajadurai, T. Christopher, G. Thanigaiyarasu, B. Rao, Finite element analysis with an improved failure criterion for composite wind turbine blades, Forsch. Im Ingenieurwesen 72 (2008) 193–207, http://dx.doi.org/10.1007/s10010-008-0078-8.
[30] L. Overgaard, E. Lund, O. Thomsen, Structural collapse of a wind turbine blade. Part a: Static test and equivalent single layered models, Compos. Part A: Appl. Sci. Manuf. 41 (2010) 257–270, http://dx.doi.org/10.1016/j.compositesa.2009.10.011.
[31] P. Harper, S. Hallett, Advanced numerical modelling techniques for the structural design of composite tidal turbine blades, Ocean. Eng. 96 (2015) 272–283, http://dx.doi.org/10.1016/j.oceaneng.2014.12.025.
[32] D. Corren, J. Colby, M. Adonizio, Improved Structure and Fabrication of Large, High-Power KHPS Rotors - Final Scientific/Technical Report, Verdant Power, Inc, New York, NY United States, 2013, http://dx.doi.org/10.2172/1084212.
[33] O. De la Torre, D. Moore, D. Gavigan, J. Goggins, Accelerated life testing study of a novel tidal turbine blade attachment, Int. J. Fatigue 114 (2018) 226–237, http://dx.doi.org/10.1016/J.IJFATIGUE.2018.05.029.
[34] H. Gonabadi, A. Oila, A. Yadav, S. Bull, Structural performance of composite tidal turbine blades, Compos. Struct. 278 (2021) 114679, http://dx.doi.org/10.1016/j.compstruct.2021.114679.
[35] C. Glennon, W. Finnegan, N. Kaufmann, P. Meier, Y. Jiang, R. Starzmann, J. Goggins, Tidal stream to mainstream: Mechanical testing of composite tidal stream blades to de-risk operational design life, J. Ocean. Eng. Mar. Energy 8 (2022) 163–182, http://dx.doi.org/10.1007/s40722-022-00223-4.
[36] W. Finnegan, Y. Jiang, P. Meier, L. Hung, E. Fagan, F. Wallace, C. Glennon, M. Flanagan, T. Flanagan, J. Goggins, Numerical modelling, manufacture and structural testing of a full-scale 1 MW tidal turbine blade, Ocean. Eng. 266 (2022) 112717, http://dx.doi.org/10.1016/j.oceaneng.2022.112717.
[37] Y. Jiang, W. Finnegan, F. Wallace, M. Flanagan, T. Flanagan, J. Goggins, Structural analysis of a fibre-reinforced composite blade for a 1 MW tidal turbine rotor under degradation of seawater, J. Ocean. Eng. Mar. Energy 9 (2023) 477–494, http://dx.doi.org/10.1007/s40722-023-00279-w.
[38] P. Davies, N. Dumergue, M. Arhant, E. Nicolas, S. Paboeuf, P. Mayorga, Material and structural testing to improve composite tidal turbine blade reliability, Int. Mar. Energy J. 5 (2022) 57–65, http://dx.doi.org/10.36688/imej.5.57-65.
[39] S. Lopez Dubon, F. Cuthill, C. Vogel, C. Ó Brádaigh, E. McCarthy, A full-scale composite tidal blade fatigue test using single and multiple actuators, Compos. Part A: Appl. Sci. Manuf. 181 (2024) 108140, http://dx.doi.org/10.1016/j.compositesa.2024.108140.
[40] S. Lopez Dubon, C. Vogel, D. Garcia Cava, F. Cuthill, E. McCarthy, C. Ó Bradaigh, A full-scale tidal blade fatigue test using the FastBlade facility, Renew. Energy 228 (2024) 120653, http://dx.doi.org/10.1016/j.renene.2024.120653.
[41] M. Valdivia-Camacho, S. Lopez Dubon, F. Cuthill, M. Munko, E. McCarthy, P. Alam, C. Ó Brádaigh, Clamping parameters in full-scale tidal turbine blade tests: A case study, Ocean. Eng. 327 (2025) 120722, http://dx.doi.org/10.1016/j.oceaneng.2025.120722.
[42] IEC iec TS 62600-202:2022, 2022.
[43] DNV GL DNVGL-ST-0164: Tidal turbines, 2022.
[44] B. Sellar, C. Old, D. Ingram, Field-Measurements Aligned To the Implementation of a Tidal Energy Converter's Power Performance Assessment, IEC 62600-200 PPA Type A, University of Edinburgh. School of Engineering, 2022, http://dx.doi.org/10.7488/ds/3448.
[45] C. Huxley-Reynard, J. Thake, G. Gibberd, TG-RE-040-0091 Rev B Deepgen Blade Design Report, 2008.
[46] V. Ramírez-Elías, N. Damian-Escoto, K. Choo, M. Gómez-Martínez, A. Balvantín-García, J. Peña, Structural analysis of carbon fiber 3D-printed ribs for small wind turbine blades, Polymers 14 (2022) 4925, http://dx.doi.org/10.3390/polym14224925.
[47] D. Zhu, R. Tao, Z. Lu, Y. Wu, R. Xiao, Optimization design of the internal structural support of marine turbine blade for weight reduction: A preliminary study, Ocean. Eng. 260 (2022) 111989, http://dx.doi.org/10.1016/j.oceaneng.2022.111989.
[48] M. Jureczko, M. Pawlak, A. Mężyk, Optimisation of wind turbine blades, J. Mater. Process. Technol. 167 (2005) 463–471, http://dx.doi.org/10.1016/j.jmatprotec.2005.06.055.
[49] L. Forcier, S. Joncas, Development of a structural optimization strategy for the design of next generation large thermoplastic wind turbine blades, Struct. Multidiscip. Optim. 45 (2012) 889–906, http://dx.doi.org/10.1007/s00158-011-0722-z.
[50] I. Kuznetsov, V. Kozhin, A. Novokshenov, T. Elsken, A. Nemov, Optimization approach for the core structure of a wind turbine blade, Struct. Multidiscip. Optim. 67 (2024) 108, http://dx.doi.org/10.1007/s00158-024-03812-z.

[51] J. Mishnaevsky, Current challenges of wind energy development: Materials science aspects, Phys. Mesomech. 24 (2021) 533–540, http://dx.doi.org/10.1134/S1029959921050040.
[52] A. Calabrese, A. Vassilopoulos, On the fatigue behavior of thin and thick adhesively bonded composite joints, Int. J. Fatigue 199 (2025) 109065, http://dx.doi.org/10.1016/j.ijfatigue.2025.109065.
[53] S. Feih, H. Shercliff, Adhesive and composite failure prediction of single-l joint structures under tensile loading, int. J. Adhes. Adhes. 25 (2005) 47–59, http://dx.doi.org/10.1016/j.ijadhadh.2004.02.005.
[54] C. Innis, T. Pardoen, Thickness-dependent selection of adhesive joints, J. Adhes. 100 (2024) 1155–1208, http://dx.doi.org/10.1080/00218464.2023.2294131.
[55] D. Srinivasan, A. Vassilopoulos, Toughening of thick bonded interfaces through architected crack-arresting features, Compos. Part A: Appl. Sci. Manuf. 188 (2025) 108575, http://dx.doi.org/10.1016/j.compositesa.2024.108575.
[56] A. Akhavan-Safar, M. Ayatollahi, L. Silva, Strength prediction of adhesively bonded single lap joints with different bondline thicknesses: A critical longitudinal strain approach, Int. J. Solids Struct. 109 (2017) 189–198, http://dx.doi.org/10.1016/j.ijsolstr.2017.01.022.